Simulation-aided geotechnical site investigation

Lluís Monforte[1#], *Marcos* Arroyo[1,2], and *Antonio* Gens[1,2]

[1]*Centre Internacional de Mètodes Numèrics en Enginyeria (CIMNE), Spain*
[2]*Universitat Politècnica de Catalunya (UPC-BarcelonaTECH), Spain*
[#]*Corresponding author: lluis.monforte@upc.edu*

ABSTRACT

With the advancement of computational geomechanics over the past decades, most of the activities typical of site characterization, such as in situ testing or sampling, can be realistically simulated using appropriate constitutive models and balance equations for geomaterials. These numerical simulations are not only informative of the processes that take place during testing but can be used to assess the reliability of current practice empirical interpretation techniques or even propose new interpretation techniques.
In this paper, we present two numerical analyses of long-standing geotechnical problems in which new insights are gained by means of advanced numerical modelling. The first analysis corresponds to cone penetration testing in undrained, brittle geomaterials; we describe the effect of the constitutive parameters on cone metrics, and we propose a novel procedure to estimate the initial state parameter from CPTu based on a wide-ranging parametric analysis. The second analysis involves tube sampling in undrained geomaterials. A total stress analysis allows us to describe the kinematics of the soil during tube insertion and evaluate the effect of the tube geometry on the strain path of the problem. The analysis is then extended by considering a fully coupled hydromechanical formulation and a critical state constitutive model for cemented soils; by simulating conventional laboratory tests on the soil that has entered the tube we can quantify sampling disturbance in terms of geotechnical design parameters (e.g. undrained shear strength and yield stress).
The possibilities offered by numerical modelling for site characterization are far from being fully exploited. It is envisaged that in the future site-specific numerical analyses will become available, enabling a more comprehensive understanding of the subsurface conditions.

Keywords: Numerical modelling; CPTu; state parameter; sampling disturbance.

1. Introduction

Site characterization is an activity in which uncertainties of a diverse nature are present. One of the contributing uncertainties is that most interpretation techniques of in situ tests are, to a large extent, still based on empirical approaches, supported by experience and well-documented databases. With the advancement of numerical methods, it is now possible to numerically simulate typical activities of site investigation (such as sampling or in situ testing) employing adequate constitutive laws, governing equations and considering all geometrical aspects of the problem in hand. These numerical analyses not only provide full details on the mechanisms underlying in situ testing, such as the stress and strain path of the soil during the test or the prevailing plastic failure mechanism but can also be used to assess the reliability of interpretation techniques currently used in practice or even propose new ones.

Without being exhaustive, numerical analyses of cone penetration testing have been used to study the cone factors of fine grained soils (Lu et al. 2004; Walker and Yu 2006; Sheng et al. 2013), quantify the effect of soil layering on the cone response (van den Berg et al. 1996; Walker and Yu 2010; Boschi et al. 2024), show the effect of drainage conditions on the cone response (Sheng et al. 2014; Ceccato et al. 2016; Monforte et al 2018b), simulate cone dissipation testing (Ansari et al. 2014), explore the relation between the state parameter and cone metrics (Martinelli and Pisanò 2022; Monforte et al. 2023a; Mozaffari and Ghafghazi 2023) or even study the dynamic effects during free-fall cone testing (Nazem et al. 2012; Zambrano-Cruzatty and Yerro 2020), among others. The complexity of the governing equations and the assumed constitutive response of soil ranges from total stress analyses using an associated, perfectly plastic Tresca model (Monforte et al. 2017a) to hydro-mechanical formulations using critical state models such as the Modified Cam Clay (Sheng et al. 2014), state parameter dependent models (Monforte et al. 2021; Mozaffari and Ghafghazi 2023) and even state parameter dependent models that account for the effect of cementation (Hauser and Schweiger 2021, 2023).

The Finite Element method, which has been successfully applied to solve coupled hydro-mechanical problems in geotechnical engineering for more than four decades (as shown by early papers in the 1980s, for instance Vermeer and Verruijt (1981)), becomes unreliable once geometric nonlinearities intervene (as is the case of cone penetration testing): in Lagrangian formulations, the mesh becomes highly distorted, leading to inaccurate results, loss of convergence of the global problem and calculation stoppage (De Borst and Vermeer, 1984). Thus, simulation of activities typical of site investigation call for advanced numerical techniques. Among others, the Material Point method (MPM) (Ceccato et al. 2016; Martinelli and Galavi, 2021; Yost et

al, 2022), the Arbitrary Lagrangian Eulerian (ALE) (van den Berg et al. 1996; Nazem et al. 2008, 2012), RITTS (Hu and Randolph 1996; Lu et al. 2004; Zhou et al. 2009) or the Particle Finite Element method (Monforte et al, 2017b) have been employed.

Of course, not all simulations of in situ tests have been conducted by means of continuum methods. The Discrete Element method (Cundall and Strack 1979) has been employed to simulate cone penetration testing in sands (Lobo-Guerrero and Vallejo 2005; Arroyo et al. 2011; Butlanska et al. 2014; Khosravi et al. 2020), even considering grain crushing (Ciantia et al. 2016), or the standard penetration test in granular materials (Zhang et al, 2019; 2021), to name a few.

The objective of this paper is to present a brief summary of some recent work carried out by our research group regarding the modelling of insertion problems relevant to site characterization employing a continuum-based numerical approach. This paper first reviews the basic features of PFEM numerical procedures. Then, the focus is placed on the numerical analysis of two insertion problems, namely cone penetration testing in liquefiable soils and soil disturbance due to tube sampling. In both cases, full details of the stress and strain path of the soil induced by the insertion of the rigid structure are given. In the first case, the numerical analyses of CPTu in liquefiable soils allows us to explore the effect of brittleness of the soil on the cone factors and to propose a new interpretation of the state parameter, both in practically undrained conditions. In the second case, the simulations of tube sampling give new insights on the strain path undergone by the soil that enters the sampler; moreover, these numerical simulations enable us to quantify -in terms of design parameters- the disturbance caused by tube sampling and explore in a systematic way the effect of different sampler geometries.

2. Particle Finite Element method (PFEM)

The Particle Finite Element method (PFEM) (Oñate et al. 2004; Idelsohn et al. 2004) is a computational method well suited for the numerical analysis of coupled multi-physics problems in which the domain suffers large deformations, rotations, and displacements. The method was first developed to solve fluid-structure interaction problems (Oñate et al. 2004) and has been extended to other areas, as solid-solid interaction and thermo-plastic problems (Oliver et al. 2005; Rodríguez et al. 2016), tool-rock interaction in the area of tunnelling (Carbonell et al. 2010; 2013) or granular flow (Zhang et al, 2013, 2014), among others.

PFEM is a continuum-based method that employs a Lagrangian description of motion and borrows concepts of particle discretization methods. On the one hand, the solution is computed with the Finite Element method, employing an Updated Lagrangian approach and typically discretising the continuum with linear elements (linear triangles in 2 dimensional simulations and linear tetrahedral elements in 3 dimensional cases). On the other hand, the discretization is continuously re-meshed to avoid the numerical problems that arise in Lagrangian Finite Element method (FEM) once the mesh gets severely distorted (or even tangled) due to the deformation of the medium. It is in this remeshing step when the nodes of the Finite Element mesh serve as particles: a new finite element mesh is constructed by performing a new Delaunay tessellation preserving the current position of the nodes/particles and, moreover, the boundary of the domain is identified based on the particle distribution using suitable methods. It should be emphasized that the use of a Delaunay tessellation assures good geometric quality of the finite element mesh. Moreover, in the present implementation h-adaptive techniques are employed to obtain a better discretization of the domain (Rodriguez et al. 2016; Carbonell et al. 2022). New particles are introduced in areas where plastic strains are large, so the failure plastic mechanism can be accurately captured. Conversely, nodes might be removed in regions in elastic regime, as a high number of nodes is not required to obtain an accurate solution.

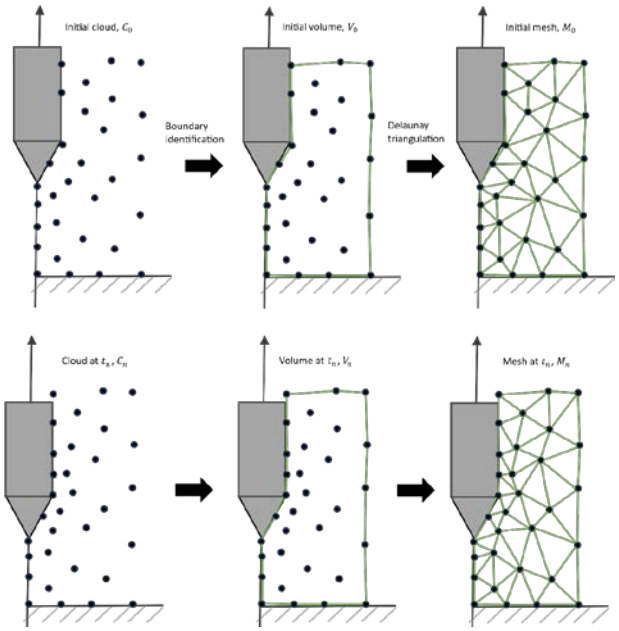

Figure 1. Sequence of steps to update in time a cloud of nodes presenting a soil mass that is progressively deformed due to the penetration of a rigid object.

A typical simulation involves the following steps (Oñate et al. 2004), which are graphically illustrated in Figure 1:

1. Begin the calculation of each time step with a cloud of particles defining the domain.
2. Identification of the boundaries of the domain. Typically, this is done using an α-shape method (Edelsbrummer and Mücke 1994) or the boundary of the previous is preserved. Transfer the boundary conditions of the previous boundary to the new one.
3. Discretize the domain in a finite element mesh using a Delaunay tessellation. Transfer the nodal and elemental information from the previous mesh to the new one using suitable methods.
4. Solve the governing equations for one time-step.
5. Update the position of the nodes of the mesh.
6. Introduce or remove nodes based on the evolution of plastic variables.

7. Go back to the first step of this cycle and repeat for the next time-step.

The contact constraints between the soil and the structure are introduced to the solution by means of a penalty approach (Wriggers 2006). Moreover, as the stiffness of the structure is several orders of magnitude larger than the stiffness of the soil, it is assumed that the structure is completely rigid. In the simulations reported herein and to further simplify the numerical formulation, it is assumed that the structure can be discretized as a smooth parametric surface, whose displacements in time are known beforehand.

FEM and PFEM suffer from several numerical pathologies that need to be addressed using advanced numerical techniques. As PFEM is well rooted on FEM, classical FEM techniques to address such numerical pathologies are directly incorporated into the PFEM procedures.

In the present implementation, all nodal fields (displacement, water pressure, etc …) are discretized with the same linear shape functions, which give rise to two distinct pathologies, namely unstable response in the undrained limit and volumetric locking.

In hydromechanical simulations, the solution becomes unstable in practically undrained conditions, as Babuska-Brezzy conditions are not fulfilled (Zienkiewicz et al. 1999); this results in high amplitude, unphysical oscillations of the pore-pressure field (Vermeer and Verruijt 1981). This numerical pathology is alleviated by adding a stabilization term (Bochev et al. 2006; Monforte et al. 2017b, 2018a).

Linear elements present volumetric locking once the constitutive response tends to incompressibility (Zienkiewicz et al. 2013). In coupled hydromechanical simulations this situation arises at critical state; in total stress analysis both elastic and elasto-plastic regime results in a practically incompressible response (Sun et al. 2013). Volumetric locking causes an over-stiff solution and stress fields present a checkerboard pattern. In PFEM, this numerical pathology is mitigated by using a mixed, stabilized formulation. For this purpose, an additional balance equation and nodal variable is introduced into the governing equations (such as the mean effective stress or the volume change) and an additional stabilization term is added to the additional balance equation (Monforte et al. 2017a).

Another pathology, this one affecting both low and high order finite elements, is the mesh dependence of the solution once strains localize in softening-dominated simulations (Bažant and Jirásek 2003). This pathology is mitigated by employing an integral-type non-local regularization technique (Galavi and Schweiger 2010; Mánica et al. 2018; Monforte et al. 2019).

The simulations of insertion problems are highly non-linear: the material response is described with non-associate elasto-plastic models and the contact algorithms, the mixed formulations and using a large-strain formulation of the global balance equation add further non-linearities to the problem. Thus, convergence of the non-linear solver employed to solve the global problem might be challenging. To increase the robustness of this non-linear solver and reduce the sources of non-linearities, the explicit stress integration technique for large-strains elasto-plastic models based on Sloan et al (2001) (Monforte et al. 2015) is embedded into the more versatile IMPLEX technique (Oliver et al. 2008). Further details can be found in Monforte et al. (2019).

3. Cone penetration testing in undrained, liquefiable materials

In the last decades, mining has been in an unprecedented expansive phase globally. During the mineral extraction process, most of the crushed rock represents waste material. Despite recent advances in recycling of tailing resources, the volume of tailings produced every year is increasing. These tailings are stored by means of tailing dams or tailing storage facilities (TSF). Even if the same principles of soil mechanics typically used to design other types of dams can be used to design TSF, mine tailings typically exhibit a brittle, contractive behavior, and are thus susceptible to static liquefaction (Fourie et al. 2022). This brittle response is responsible for the large number of dam failures; compared to conventional retention dams, the tailing impoundment failure is approximately ten times greater (Davies et al. 2002).

The design of tailing dams is hampered by the lack of adequate methods to evaluate the strength of these tailings and their susceptibility to liquefaction. Even if the mechanical constitutive response of tailings could be evaluated by performing conventional laboratory tests, the extraction of good quality samples is unfeasible, as sampling these loose and soft soils produces irreversible changes to their state. Therefore, these materials are frequently characterized by in situ tests, especially cone penetration testing (CPTu). Even if the interpretation of CPTu in the vast majority of soils is mature, advice on the interpretation of the test in these geomaterials with a meta-stable structure is still uncertain.

The susceptibility to liquefaction and the state of soils with a meta-stable structure is frequently described by the state parameter (Been and Jefferies 1985), defined as the current void ratio minus the void ratio at critical state conditions at the same mean effective stress. Consequently, a negative state parameter denotes a soil whose void ratio is below the critical state line and, once loaded in undrained conditions, will exhibit a dilatant behavior. Conversely, a soil with a positive state parameter has a void ratio above the critical state line and will exhibit a contractive behavior and is susceptible to liquefaction.

A number of techniques have been proposed for deriving the in situ state parameter from cone metrics. Under undrained cone penetration, these techniques relate the normalized effective tip resistance, $Q_p\big(1 - B_q\big) + 1$, to the in-situ state parameter, ψ_0, using two fitting variables ($\overline{k}$ and $\overline{m}$):

$$Q_p\big(1 - B_q\big) + 1 = \frac{q_t - u_2}{p'_0} = \overline{k}\exp(-\overline{m}\,\psi_0) \qquad (1)$$

The value of the fitting variables, $\overline{k}$ and $\overline{m}$, are soil specific. The relation between the fitting parameters and critical state parameters of the soil has been established by means of empirical relations (Plewes et al, 1992; Jefferies and Been 2015), cavity expansion solutions

(Shuttle and Cunning 2007; Shuttle and Jefferies 2016; Mo et al. 2024) and numerical simulation (Pezeshki and Ahmadi 2022, Monforte et al. 2023a).

The aim of this section is to report a set of numerical analysis of cone penetration testing in undrained conditions (Monforte et al 2021) and develop a state parameter interpretation technique based on the numerical results (Monforte et al 2023a,b). After briefly describing the employed constitutive relation and describing the adopted constitutive parameters, we report and discuss the results of a wide ranging parametric analysis. Finally, we present the new interpretation technique, which is based on the modification of a cavity expansion solution based on the differences of the stress state around a penetrating cone and an expanding spherical cavity.

3.1. Constitutive model: CASM

The constitutive response of the soil is modelled using CASM (Yu 1998), a critical state-based, state parameter dependent constitutive model. Roughly speaking, CASM can be understood as a modified version of the Cam Clay family of constitutive models, in which two additional constitutive parameters are introduced. These two parameters modify the shape of the yield surface in the stress space and control the relative distance (in terms of void ratio) between the isotropic compression line and the critical state line (in the compression plane). These two extra parameters add more flexibility to the constitutive model and allow the representation of a wide range of soil behaviors, including softening, ductile or dilation materials (Yu 1998).

The constitutive model has been implemented using a large-strain elasto-plastic framework in which the deformation gradient splits multiplicatively into an elastic and plastic part (Simo and Hughes 1998) and in general stress space. For the sake of simplicity, the constitutive model is briefly described here in terms of stress invariants.

The yield surface of the model is described by:

$$f = \left(\frac{q}{Mp'}\right)^n + \frac{1}{\ln(r)}\ln\left(\frac{p'}{p_c}\right) \tag{2}$$

where p' is the mean effectives stress, q is the deviatoric stress, p_c is the preconsolidation stress, and M is the stress ratio at critical state, that for conditions different from triaxial compression depends on the Lode's Angle according to a smoothed Mohr-Coulomb failure criterion (Abbo and Sloan 1995). n and r are two constitutive parameters that control the shape of the yield surface.

As in the Cam Clay model, a classical isotropic volumetric hardening rule governs the evolution of the preconsolidation stress:

$$\dot{p}_c = \frac{p_c}{\lambda^\star - \kappa^\star}\,\dot{\epsilon}_v^p \tag{3}$$

where $\lambda^\star = \frac{\lambda}{1+e_0}$, λ is the slope of the isotropic compression line and the critical state line in the compression plane, $\kappa^\star = \frac{\kappa}{1+e_0}$, κ is the slope of the reloading curve and $\dot{\epsilon}_v^p$ stands for the temporal derivative of the plastic volumetric strains.

The model is non-associated, and the flow rule proposed by Mánica et al (2021, 2022) is employed. The dilatancy rule (for triaxial compression conditions) reads:

$$d^p = \frac{m-1}{m}\frac{M^m - \eta^m}{\eta^{m-1}} \tag{4}$$

where m is a constitutive parameter of the model, $\eta = q/p'$ is the stress ratio and d^p is the dilatancy: the ratio of incremental plastic volumetric strains to plastic deviatoric shear strains.

Using some of the previous expressions, it can be shown that the isotropic compression line and critical state line can be expressed as:

$$e = e_0 - \lambda \ln\left(\frac{p'}{p_r}\right) \tag{5}$$

$$\Gamma = [e_0 - (\lambda - \kappa)\ln(r)] - \lambda \ln\left(\frac{p'}{p_r}\right) \tag{6}$$

where e and Γ are the void ratio at the isotropic compression line and critical state line, respectively. The void ratio at the isotropic line is equal to e_0 at the reference mean effective stress p_r.

As the critical state line of the model is a straight in the $e - \ln(p')$ plane, the residual undrained shear strength, S_u^{res}, can be explicitly evaluated from the initial state parameter of the soil, ψ_0, the initial mean effective stress, p'_0, and critical state constitutive parameters of the soil, λ and M, as:

$$S_u^{res} = \frac{M}{2}\,p'_0 \exp\left(-\frac{\psi}{\lambda}\right) \tag{7}$$

Here, the critical state undrained shear strength is denoted as residual undrained shear strength, as the focus of this section is placed in liquefiable materials.

As it will be used below, let us recall the definition of the Bishop's brittleness index as:

$$I_b = \frac{S_u^{peak} - S_u^{res}}{S_u^{peak}} \tag{8}$$

being S_u^{peak} the peak undrained shear strength.

3.2. Spherical cavity expansion solution

The results of the numerical analysis of cone penetration testing will be compared to the predictions of cavity expansion. Moreover, the similitudes and discrepancies of the numerical results of CPTu and the analytical solution of a spherical cavity expansion will play a pivotal role in the proposal of a new technique for the inversion of the state parameter from CPTu metrics during undrained insertion.

In this work, the expressions for the total cavity resistance and excess pore pressure proposed by Mo and Yu (2017) for the infinite expansion of a spherical cavity are employed. These analytical solutions have been obtained for CASM, assuming a different flow rule than that employed in the present work.

The effective stress state at the wall of the cavity, however, is evaluated with a more general expression, the only assumptions are that (i) the constitutive response of the soil can be described by a critical state soil model and (ii) the expansion of the cavity is large enough to induce critical state conditions to the soil at the wall of cavity.

The expansion of a spherical cavity on a soil whose initial stress state is isotropic loads the soil in triaxial compression conditions; the radial effective stress, σ'_r, is the major principal stress; the other two principal stresses are equal (see, for instance, Carter et al. 1986) and denoted here as σ'_3. Once the soil reaches critical state conditions, these stresses can be expressed as:

$$\sigma'_r = p'_{cs} + \frac{2}{3} q_{cs} \tag{9}$$

$$\sigma'_3 = p'_{cs} - \frac{1}{3} q_{cs} \tag{10}$$

where p'_{cs} is the mean effective stress at critical state conditions and q_{cs} is the deviatoric stress at critical state conditions. These two stress invariants can be expressed in terms of the residual (critical state) undrained shear strength, S_u^{res}, as $p'_{cs} = q_{cs}/M = 2\ S_u^{res}/M$ (where M is the stress ratio at critical state corresponding to triaxial compression conditions). Therefore, the two previous equations can be rewritten as:

$$\sigma'_r = \left(\frac{2}{M} + \frac{4}{3}\right) S_u^{res} \tag{11}$$

$$\sigma'_3 = \left(\frac{2}{M} - \frac{2}{3}\right) S_u^{res} \tag{12}$$

Finally, assuming that the critical state line is straight in the $e - \ln(p')$ plane, and thus introducing Equation (7), the following expressions can be obtained for the effective stress state of the soil around a spherical cavity whose expansion has been large enough to induce critical state conditions on the soil around the cavity:

$$\sigma'_r = \left(1 + \frac{2M}{3}\right) p'_0 \exp\left(-\frac{\psi}{\lambda}\right) \tag{13}$$

$$\sigma'_3 = \left(1 - \frac{M}{3}\right) p'_0 \exp\left(-\frac{\psi}{\lambda}\right) \tag{14}$$

Thus:

$$\frac{\sigma'_c}{p'_0} = \frac{\sigma_c - u}{p'_0} = \left(1 + \frac{2M}{3}\right) \exp\left(-\frac{\psi}{\lambda}\right) \tag{15}$$

Therefore, Equation (15) expresses the effective resistance of a spherical cavity under very basic hypotheses: (i) the expansion induces critical state at the soil around the wall of the cavity and (ii) the critical state line is described by a straight line in the $e - \ln(p')$ plane.

It should be noted that the expression usually employed to invert the state parameter, Equation (1), which was originally proposed based on empirical considerations, has the same formal structure as the expression developed for the expansion of a spherical cavity that induces critical state conditions to the soil at the wall of the cavity.

3.3. CPTu: representative numerical results

3.3.1. Description of the numerical model

Due to the symmetry of cone penetration testing, an axisymmetric model is employed. The cone has standard dimensions and is pushed at the standard rate of 2 cm/s. The size of the domain is large enough to ensure that boundary conditions have negligible effects on the numerical solution. At the vertical boundaries, null radial displacements are prescribed, whereas null displacements in all directions are prescribed at the bottom boundary. A load is placed at the upper boundary. Drainage is only allowed through the upper and lower boundaries.

All simulations are performed using a fully coupled hydromechanical formulation. In all the calculations, the value of permeability is $k = 10^{-9}$ m/s, low enough for the response of the soil to be practically undrained during CPTu testing. The effect of partial drainage on the cone response of potentially liquefiable soils is presented elsewhere (Monforte et al 2021; 2022c).

The initial vertical effective stress is set to $\sigma'_{v0} = 100$ kPa, and the horizontal effective stress is established based on Jaky's formula.

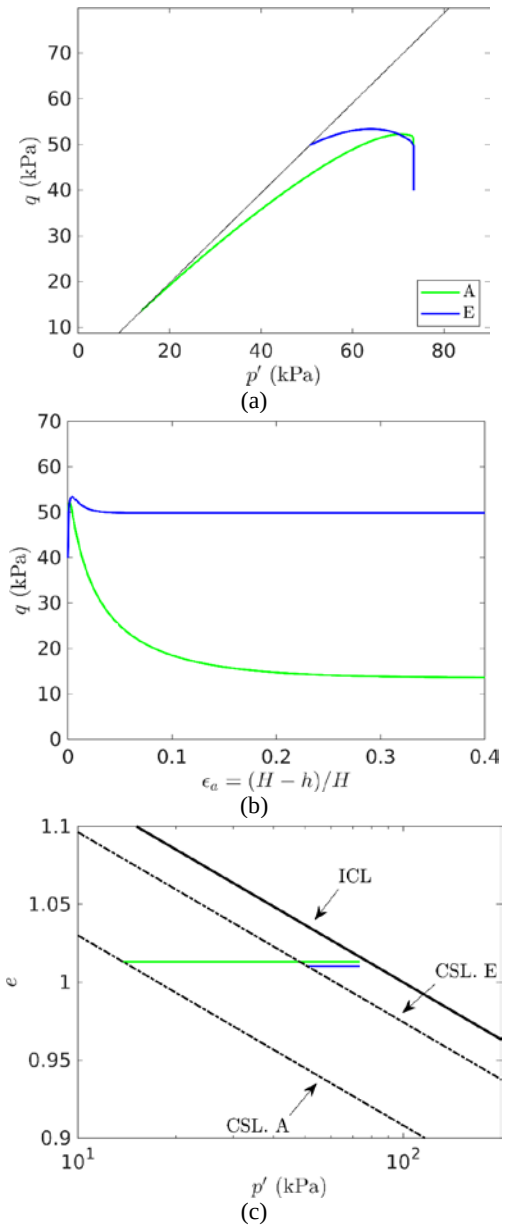

Figure 2. CPTu in undrained, liquefiable materials. Reference series. Triaxial compression testing. Results in the $p' - q$ plane, (a), evolution of deviatoric stress in terms of axial deformation, (b), and $e - \ln p'$ plane, (c).

3.3.2. Adopted constitutive parameters

The reference series of simulations consists of 5 different materials, whose peak undrained shear strength

Table 1. CPTu in undrained, liquefiable materials. Characterization of the materials and outputs of the numerical analyses (normalized cone metrics).

Series	Material	ψ_0	S_u^{peak} (kPa)	S_u^{res} (kPa)	Q_p	B_{q1}	B_{q2}	$Q_p(1-B_{q1})+1$	$Q_p(1-B_{q2})+1$
Ref	A	0.0887	26.1	6.8	1.93	1.37	1.15	0.29	0.71
	B	0.0738	26.5	9.0	2.17	1.32	1.06	0.32	0.86
	C	0.0629	26.3	11.0	2.31	1.25	1.05	0.42	0.89
	D	0.0368	26.5	18.0	2.94	1.10	0.91	0.69	1.28
	E	0.0196	26.7	24.9	3.72	0.98	0.82	1.06	1.68
OCR	A	0.0781	32.6	9.0	2.31	1.27	1.02	0.38	0.96
	B	0.0632	33.2	12.0	2.47	1.23	0.99	0.44	1.03
	C	0.0524	33.2	14.7	2.84	1.12	0.90	0.67	1.27
	D	0.0263	34.0	24.1	3.54	1.01	0.80	0.98	1.71
	E	0.0091	35.4	33.3	4.47	0.94	0.79	1.26	1.95
λ	A	0.1774	26.1	6.8	1.57	1.42	1.12	0.33	0.82
	B	0.1475	26.5	9.0	1.77	1.33	1.07	0.41	0.88
	C	0.1259	26.3	11.0	2.07	1.23	1.02	0.52	0.96
	D	0.0736	26.5	18.0	2.53	1.09	0.88	0.78	1.30
	E	0.0393	26.7	24.9	3.22	0.98	0.81	1.06	1.62
M	A	0.0882	31.7	8.2	2.20	1.33	1.12	0.27	0.73
	B	0.0734	32.2	10.9	2.55	1.24	1.03	0.40	0.93
	C	0.0625	31.9	13.4	2.77	1.19	1.00	0.48	1.01
	D	0.0362	32.2	21.9	3.68	1.04	0.86	0.85	1.51
	E	0.0187	32.7	30.6	4.65	0.98	0.81	1.07	1.87

is almost coincident, $S_u^{peak} \approx 0.26\,\sigma'_{v0}$, and they share most of the constitutive parameters, including the isotropic compression line but have different initial state parameter: therefore, each material has a different critical state line (in the $e - \ln p'$ plane) and residual undrained shear strength.

For the reference series of simulations, all materials have the same isotropic compression line, that passes through $e_0 = 1$ at an effective stress of $p_r = 100$ kPa and has a slope $\lambda = 0.054$. The stress ratio at critical state conditions is $M = 1$. The elastic response is characterized by a swelling slope of $\kappa = 0.008$ and a Poisson's coefficient of $\nu \approx 0.33$. The value of n and r is adjusted in each simulation so that all materials have a similar peak undrained shear strength.

To characterize the constitutive response of these materials, Figure 2 reports the simulation of undrained compression triaxial tests for two of the five materials: the ones with the highest and lowest initial state parameter. Of course, the initial stress state is coincident with that which will be used in the simulation of boundary value problems. Deviatoric stresses increase until reaching the peak undrained shear strength; then all materials undergo static liquefaction (i.e. undrained strain softening), reaching a residual strength of $S_u^{res} \approx 0.245\,\sigma'_{v0}$ for the material with initial state parameter of $\psi_0 = 0.020$, whereas that with an initial state parameter of $\psi_0 = 0.088$ reaches a residual strength of $S_u^{res} \approx 0.067\,\sigma'_{v0}$. Table 1 summarizes the strength ratio and initial state parameter of the three materials with intermediate state parameters.

3.3.3. Numerical results

Figure 3 reports the evolution of the net cone resistance and excess pore pressure at the u_1 and u_2 position in terms of normalized insertion depth. A clear stationary state can be observed in all cone measurements after a penetration of 10 cone radius. Material A (that with the highest state parameter) has a much lower cone resistance compared to Material E (lowest state parameter). Moreover, the state parameter also seems to have an influence on the generated excess pore pressure, even though it is more subtle.

Results of cone penetration are represented in terms of normalized parameters, namely the normalized cone tip resistance, the excess pore pressure ratio and the normalized effective tip resistance:

$$Q_p = \frac{q_t - p_0}{p'_0} \tag{16}$$

$$B_{qx} = \frac{u_x - u_0}{q_t - p_0} \tag{17}$$

$$Q_p\left(1 - B_{qx}\right) + 1 = \frac{q_t - u_x}{p'_0} \tag{18}$$

where q_t is the cone tip resistance, u_x is the pore pressure -either at the midface of the cone u_1 or at the corner

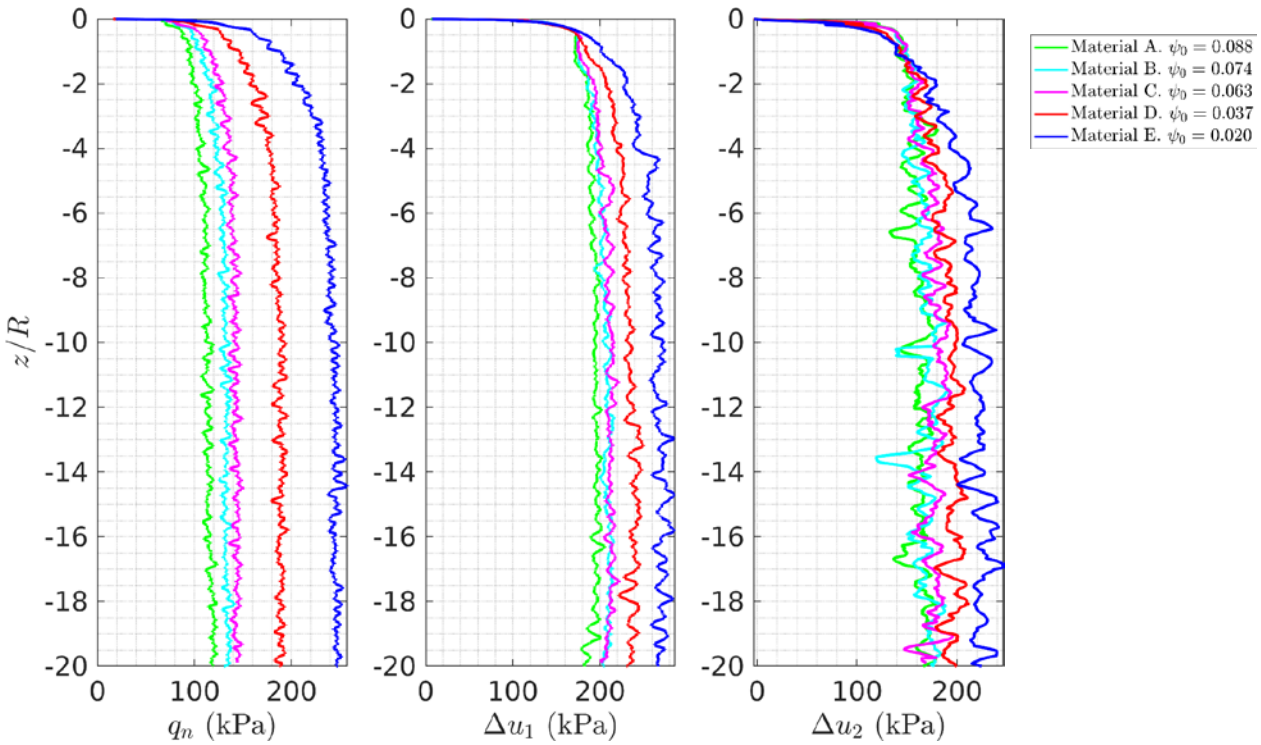

Figure 3. CPTu in undrained, liquefiable materials. Reference series. Net cone tip resistance and excess pore pressure at the midface of the cone and at the shaft in terms of depth.

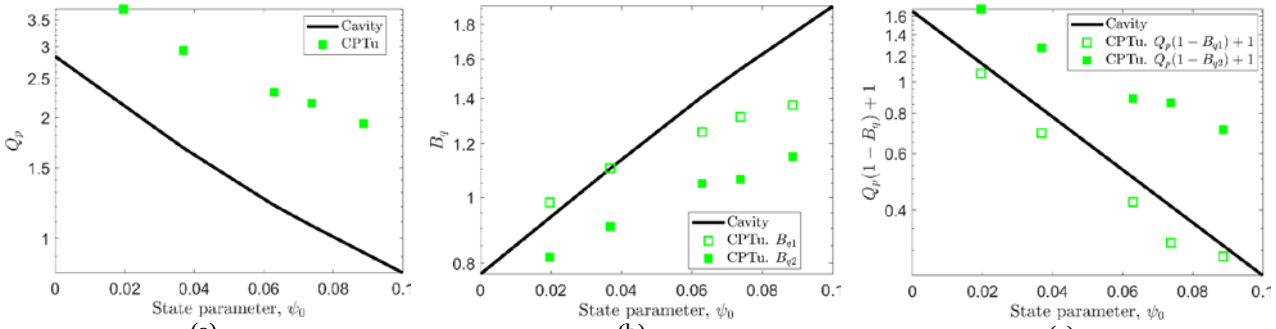

(a) (b) (c)

Figure 4. CPTu in undrained, liquefiable materials. Reference series. Normalized tip resistance, (a), Excess pore pressure ratio, (b), and normalized effective tip resistance, (c), in terms of the in situ state parameter. Comparison with a solution of spherical cavity expansion (Mo and Yu 2017).

between the cone and the shaft, u_2-, p_0' and p_0 are the effective and total in situ mean stress and u_0 is the in situ pore water pressure.

The normalized tip resistance and the normalized effective tip resistance increase as the state parameter decreases (Figure 4). Moreover, the normalized effective resistance computed with the u_1 measurement seems to depend linearly (in a semilogarithmic plot) with the state parameter. On the contrary, the excess pore pressure ratio increases with the initial state parameter. For the same state parameter, the excess pore pressure at the face of the cone is higher than that at the shoulder of the cone.

Numerical results are compared to a solution of spherical cavity expansion (Mo and Yu 2017). This analytical solution assumes that the initial stress state of the soil is isotropic (whereas CPTu simulations assumed a more realistic value of K_0) and a different flow rule than the one adopted here. In most of the metrics the same tendencies are observed: cone and cavity metrics increase or decrease with the state parameter. The differences can be explained by differences on geometry of both problems (cavity expansion vs actual geometry of cone penetration testing) with the contributing factors of different initial stress state and different flow rule. Remarkably, the normalized effective tip resistance computed with the u_1 pore pressure shows good agreement with the effective cavity resistance, Equation (15).

Figure 5 illustrates the state of the soil around the cone for Material A and Material E. In both cases, the excess pore pressure shares the same traits: the excess pore pressure is large and quite homogeneous at the tip of the cone, from where it decreases. Also, cone penetration induces liquefaction (or critical state conditions) to a broad volume of soil around the tip of the cone: there the mean effective stress and deviatoric

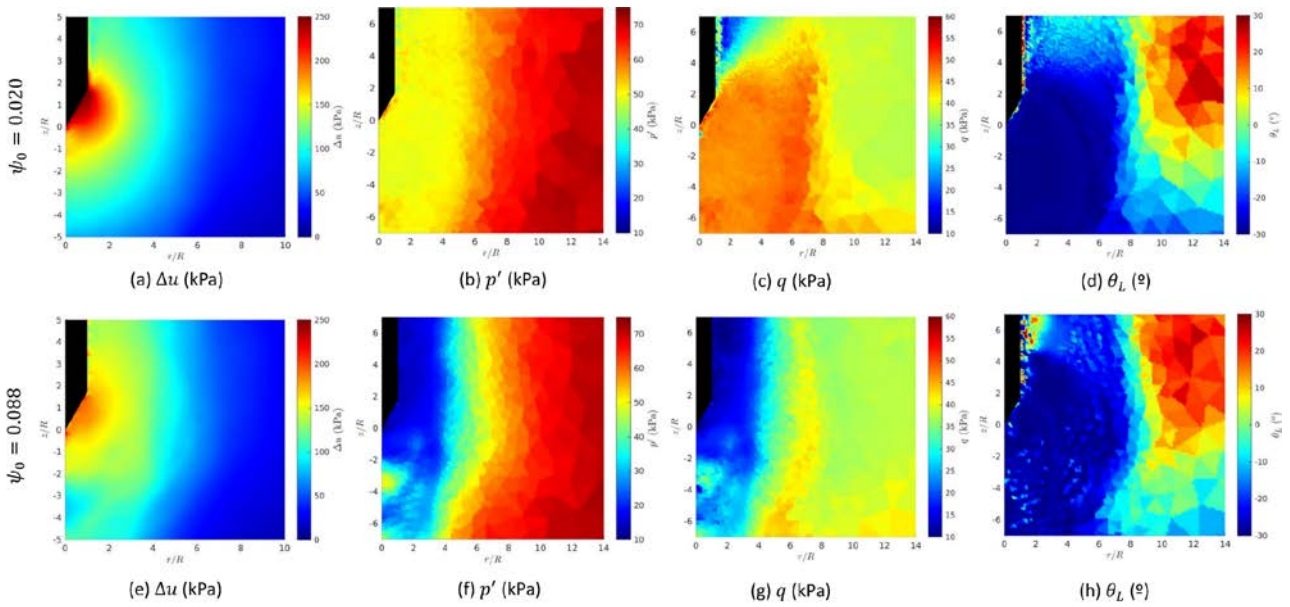

Figure 5. CPTu in undrained, liquefiable materials. Reference series. Excess water pressure and effective stress tensor invariants for two materials with different initial state parameter.

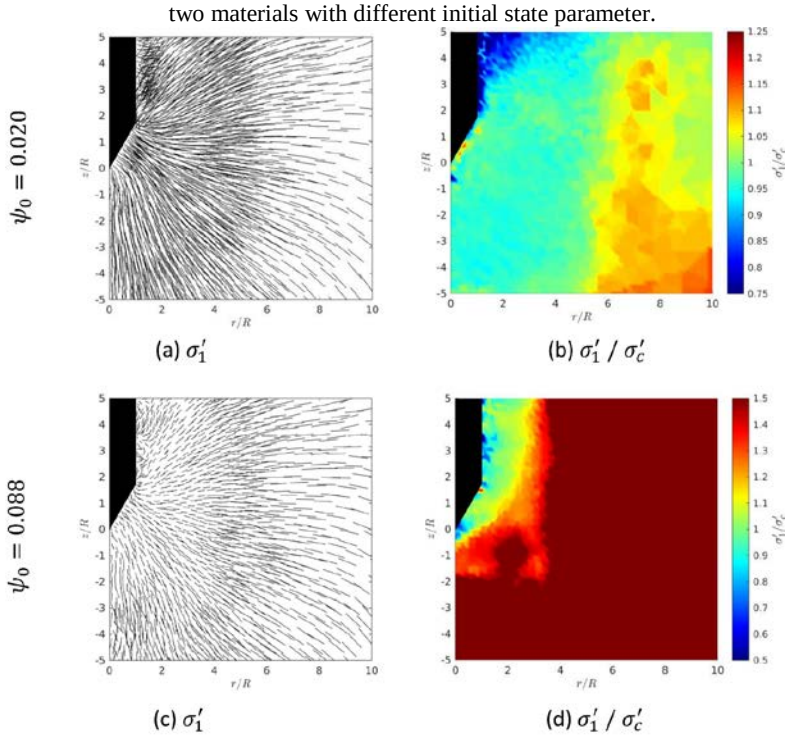

Figure 6. CPTu in undrained, liquefiable materials. Reference series. Major principal effective stress, left, and major principal effective stress scaled by the cavity effective resistance.

stresses reduce (to a very low value in Material A). Moreover, during cone penetration the soil is sheared in triaxial compression conditions (that is, the Lode's angle is almost -30º).

Finally, Figure 6 analyzes the effective stress state of the soil and compares it to that of a spherical cavity expansion. To this end, Figure 6 shows the major principal stress scaled by the principal effective stress that would result from the expansion of a spherical cavity, Equation (15). Around the tip of the cone the ratio σ_1'/σ_c' is equal to one. That is, the stress state around the tip of a CPTu and the wall of a spherical cavity (whose expansion is large) is almost coincident. In the case of a CPTu, the direction of the principal effective stress is normal to the face of the cone. This is because the cone has been assumed smooth.

A more in-depth description of the stress path of the soil, including that resulting from the insertion of a rough cone, can be found elsewhere (Monforte et al. 2021, 2023a).

3.3.4. Parametric analysis

A wide-ranging parametric analysis has been performed, to assess the effect of the soil constitutive response during undrained CPTu testing in fine grained, liquefiable materials. To this end, 3 new series of

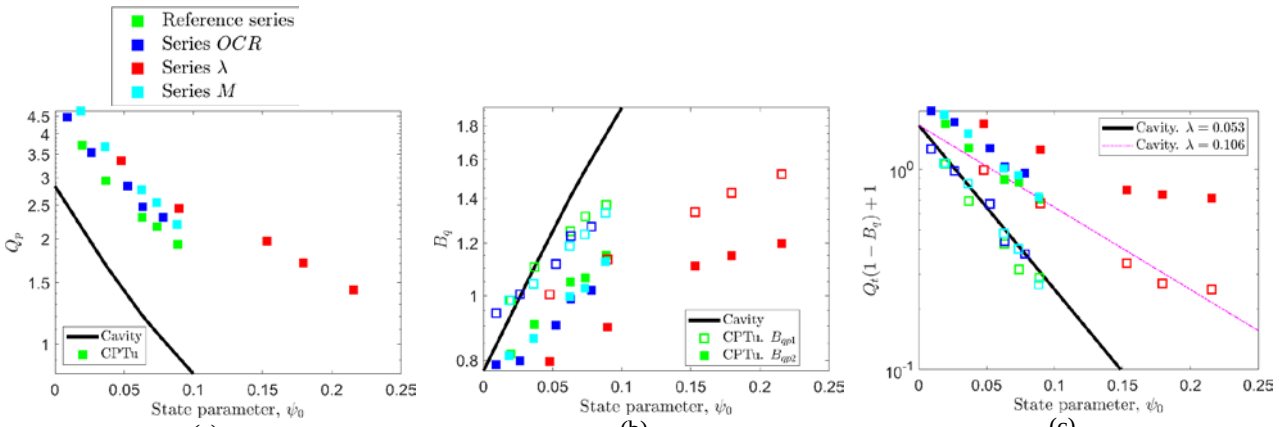

(a) (b) (c)

Figure 7. CPTu in undrained, liquefiable materials. Parametric analysis. Normalized tip resistance, (a), Excess pore pressure ratio, (b), and normalized effective tip resistance, (c), in terms of the in situ state parameter. Comparison with a solution of spherical cavity expansion (Mo and Yu 2017)

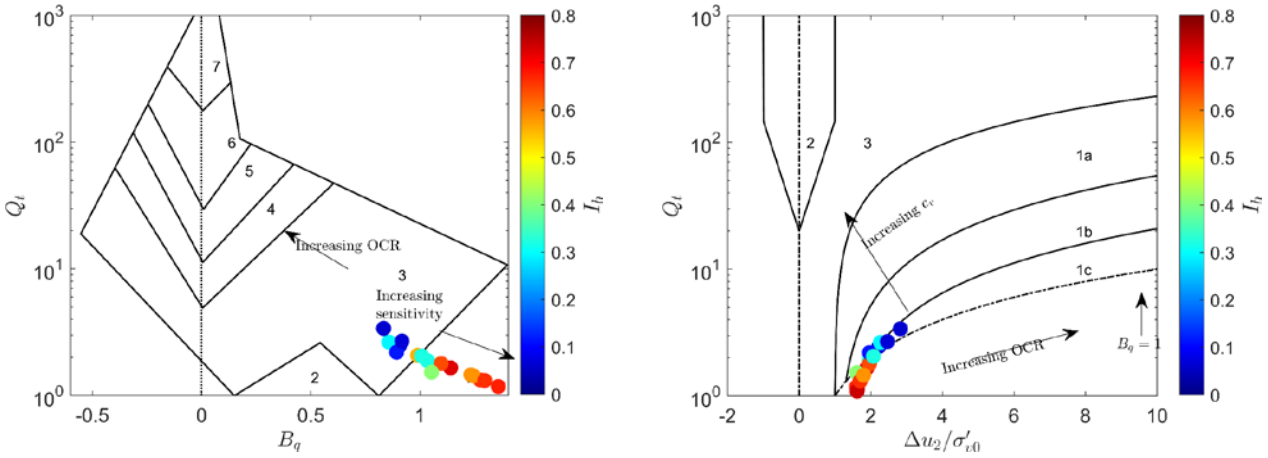

(a) Roberston (1991) (b) Schneider et al. (2008)

Figure 8. CPTu in undrained, liquefiable materials. Numerical results in custom CPTu interpretation charts: Roberston (1991), (a), and Schneider et al. (2008), (b).

simulations are presented here (other simulations can be found in Monforte et al (2023a, b)). In these series, all the constitutive parameters and initial state of the soil are those of the reference simulation except the specific parameter that is varied.

- Series M. In this set of simulations, the value of the critical state friction ratio is increased from $M = 1$ to $M = 1.33$. The value of the in situ effective horizontal stress is decreased in accordance with Jaky's expression.
- Series λ. All constitutive parameters and initial stress state of the soil are kept as in the reference simulation, but the slope of the isotropic compression line and critical state line is increased from $\lambda = 0.054$ to $\lambda = 0.108$.
- Series OCR. The over-consolidation ratio of the soil is increased from almost one to 1.5. As a result, the initial void ratio and in situ horizontal effective stress are slightly different from the reference series.

Table 1 lists the initial state parameter and the peak and residual undrained shear strength of each material.

Figure 7 shows the steady state cone metrics in terms of the initial state parameter and the brittleness parameter. Overall, the same tendencies than in the reference set of simulations are observed. It should be stressed that only the cavity expansion solution for the reference solution is reported here. All numerical simulations show a remarkable agreement between the normalized effective tip resistance computed with the u_1 and with the predictions of cavity expansion.

As in the reference set of simulations, in all simulations of this parametric analysis the stress state around the cone shares the same traits as in the reference simulations: the soil is at critical state, in triaxial compression conditions and the major principal effective stress is normal to the cone.

3.3.5. Numerical results in current practice interpretation charts

The numerical results are also reported in current practice CPTu interpretation charts, namely Roberston (1991) and Schneider et al. (2008) charts; see Figure 8. The first thing to notice is that, in both charts, simulations with almost null brittleness index plot in the expected

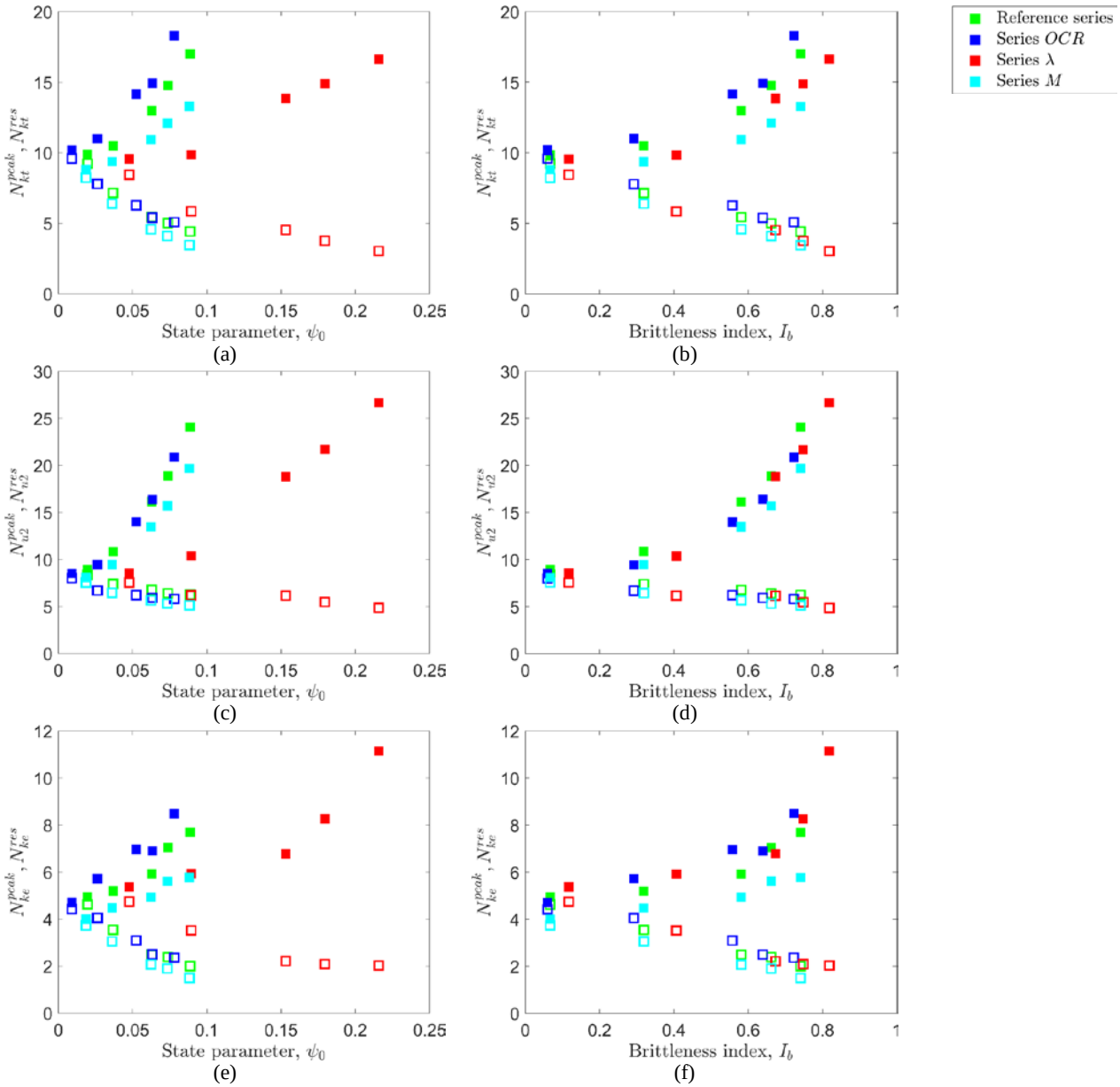

Figure 9. CPTu in undrained, liquefiable materials. Bearing capacity factors in terms of the initial state parameter, right, and brittleness index, right. $N_{kt} = \frac{q_t - \sigma_{v0}}{s_u}$, (a) and (b), $N_{u2} = \frac{u_2 - u_0}{s_u}$, (c) and (d), $N_{ke} = \frac{q_t - u_2}{s_u}$, (e) and (f). Results computed with the residual undrained shear strength are reported with colored filled symbols.

positions: those of soft, unsensitive, normally consolidated clayey materials. In Robertson chart, all numerical results plot in a straight line: by increasing the brittleness index the excess pore water pressure increases whereas the logarithm of the normalized cone tip resistance decreases, in good agreement with the empirical knowledge reflected in the chart. In Schneider chart, as the brittleness index increases, the results plot on a line corresponding to a change in over-consolidation ratio in undrained conditions.

3.3.6. Cone factors

Numerical results are further analyzed in terms of cone factors:

$$N_{kt} = \frac{q_t - \sigma_{v0}}{s_u} \tag{19}$$

$$N_{u2} = \frac{u_2 - u_0}{s_u} \tag{20}$$

$$N_{ke} = \frac{q_t - u_2}{s_u} \tag{21}$$

These three cone factors are not independent, but are related to each other through normalized cone metrics. Karslrud et al (2005) already noted the relation between two of these cone factors: $N_{u2} = B_q\, N_{kt}$. These two cone factors are also related to the third one as:

$$N_{ke} = N_{kt}\, \frac{Q_t(1-B_q)+1}{Q_t} = N_{u2}\, \frac{Q_t(1-B_q)+1}{Q_t\, B_q} \tag{22}$$

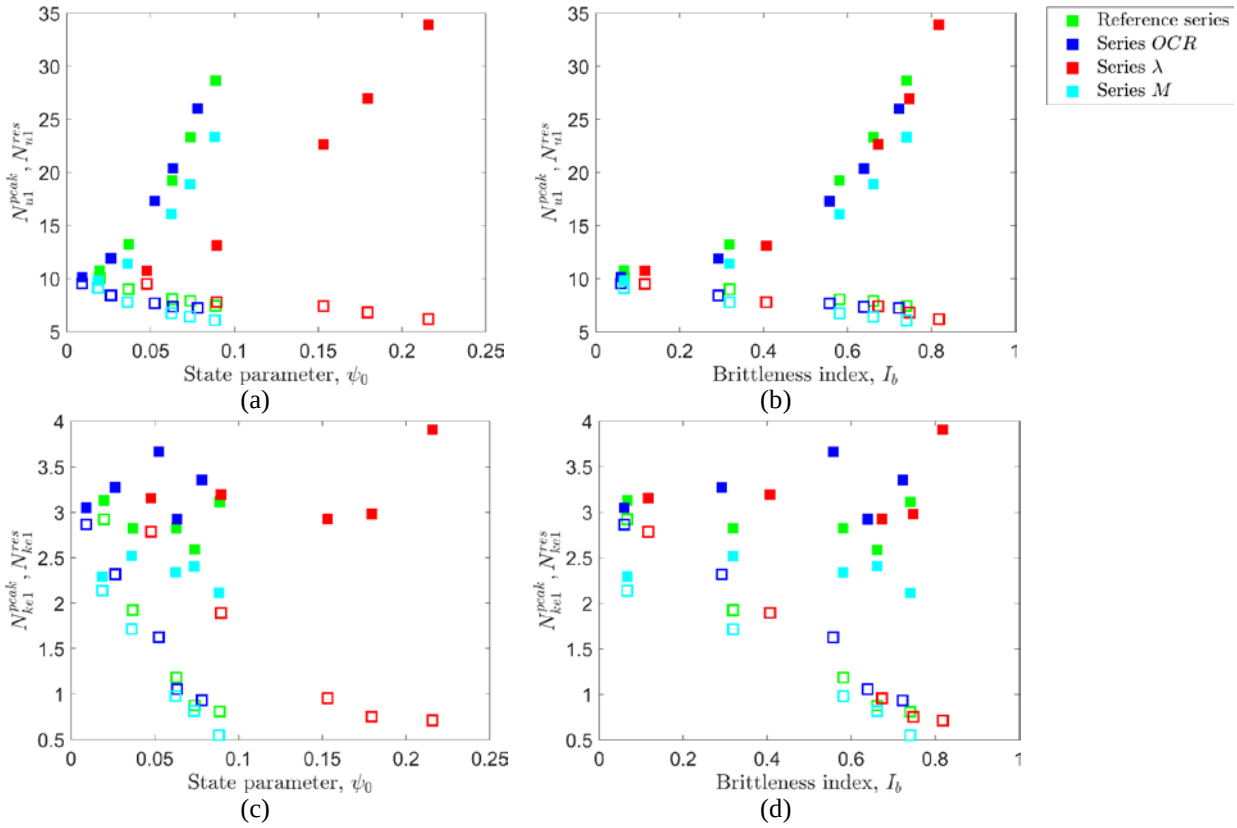

Figure 10. CPTu in undrained, liquefiable materials. Bearing capacity factors in terms of the initial state parameter, right, and brittleness index, right: $N_{u1} = \frac{u_1 - u_0}{s_u}$, (a) and (b), $N_{ke1} = \frac{q_t - u_1}{s_u}$, (c) and (d). Results computed with the residual undrained shear strength are reported with colored filled symbols.

These relations are only valid using the usual definition of cone metrics in terms of the total and effective in situ vertical stress and not using the definition with the mean stress, as in Equations (16) to (18).

As customary, in this work these cone factors are computed with the undrained shear strength during a K_0 consolidated, triaxial compression test. For each cone factor both, that corresponding to the peak and residual strength, are considered. Here, these cone factors are reported in terms of the initial state parameter and the Bishop's brittleness index.

Figure 9 and Figure 10 report the evolution of cone factors in terms of the in-situ state parameter and the brittleness index. The first thing to notice is that the N_{kt} for a brittleness index around 0 (unsensitive material) is in the range of 10, in good agreement with previous numerical simulations (Lu et al. 2004). With respect to the reference simulation, increasing the OCR leads to a moderate increase of N_{kt} whereas increasing the friction angle of the soil or increasing its compressibility leads to a moderate reduction of N_{kt}. This result can be explained by the effect that changing each constitutive parameter has on the rigidity index of the soil and on the coefficient of earth pressure at rest (as Jaky's formula is assumed). It is also consistent with current knowledge on CPTu interpretation on fine-grained soils: N_{kt} increases with the rigidity index of the soil and decreases by decreasing the in situ horizontal stress. As the state parameter of the soil (or the rigidity index) increase, N_{kt}^{peak} decreases whereas N_{kt}^{res} increases.

Similar tendencies can be observed for the cone factor defined in terms of excess pore pressure (Figure 9(c) and (d)). In this case, however, N_{u2}^{peak} shows a very gentle decrease from $N_{u2}^{peak} = 7.5$ for the almost non-brittle materials to values slightly higher than 5 for very brittle materials. This result is in good agreement with current knowledge on the interpretation of CPTu in sensitive materials: a database analysis on Norwegian sensitive clays shows that $N_{u2}^{peak} \approx 7.5$ (Paniagua et al. 2019). Equivalent results can be obtained if this cone factor is not computed with u_2 but with u_1.

Interestingly, numerical results suggest that N_{ke1}^{res} lays mostly in the range of 2.75 to 3.75 and seems independent of the brittleness (or in situ state parameter) of the soil (Figure 10(e) and (f)). On the other hand, N_{ke1}^{peak} decreases with the state parameter. If this cone metric is computed with that u_2 and not that u_1, the peak cone factor decreases with the state parameter whereas the opposite is true for the residual cone factor.

In fine grained, unsensitive soils, cone factors are a function of the rigidity index (undrained shear strength divided by the shear modulus), slightly changing with the roughness of the cone and the ratio of the vertical to horizontal in situ stress (see, for instance, Lu et al. 2004). The numerical analyses reported herein suggest that, for sensitive materials, bearing capacity factors show a strong dependence on the brittleness index of the material. If reported in terms of the state parameter, the relation between each bearing capacity factor and the state parameter depends on the slope of the CSL in the

compression plane, λ. That is to say that the cone response only depends on the initial state parameter of the soil through the residual undrained shear strength (see Equation (7)). More analyses are however required to examine the combined effect of the strain at which the peak strain is reached and the velocity of strength degradation.

The analysis also suggests that the peak undrained shear strength could be estimated using $N_{u2}^{peak} \approx 7.5$ (or alternatively $N_{u1}^{peak} \approx 10$) slightly decreasing with brittleness. Instead, a rough estimate of the residual undrained shear strength can be obtained using $N_{ke1}^{res} \approx 3.0$, but the excess pore pressure is rarely measured at the face of the cone.

Even if both observations have been obtained in a wide-ranging parametric analysis, all simulations have been performed in materials with similar peak undrained strength ratio and the effect of some constitutive parameters (for instance the shear modulus) has not been explored. Therefore, more analyses combined with field investigation are required to confirm or refine those conclusions.

3.4. State parameter inversion technique

3.4.1. Development of the inversion technique

The normalized effective resistance of a cavity and that of a CPTu, if computed with the mid-face water pressure, show a remarkable agreement. This coincidence is not fortuitous, but a consequence of the similarities between the effective stress state around an expanding cavity and a penetrating cone.

The ratio between the normalized effective tip resistance (using the u_1 pore pressure) and the effective resistance of a spherical expansion can be expressed as:

$$\frac{q_t - u_1}{\sigma_c'} = c_q \tag{23}$$

This ratio, termed here as c_q, is a geometric correction factor, as typically used to scale cavity expansion results to be used for the interpretation of cone penetration testing. Importantly, an approximate expression for c_q can be analytically derived under a number of hypotheses. The first one is that the pore pressure measured at the midface of the cone is representative of all the pore pressure acting at the face of the cone. The second hypothesis is that the effective stress field is homogeneous at the tip of the cone. Thirdly, it is assumed that the soil is at critical state in triaxial compression conditions. As shown in previous sections, these hypotheses are fulfilled to a large extent, the first two hypothesis being those that are more uncertain. Using these hypotheses and applying equilibrium of forces at the tip of the cone, it can be shown (Monforte et al. 2023a) that this term is bracketed between:

$$c_q \in \left[1, \frac{7M+6}{4M+6}\right] \tag{24}$$

being the lower limit representative of a fully smooth cone, and the upper limit of a fully rough cone. The range of this geometric correction factor is narrow: for $M = 1$ it ranges between 1 and 1.25, whereas for $M = 1.4$ the upper limit becomes 1.36.

Consequently, combining Equations (13) and (23), a first expression to invert the state parameter can be written as:

$$\frac{q_t - u_1}{p_0'} = c_q \left(1 + \frac{2M}{3}\right) \exp\left(-\frac{\psi_0}{\lambda}\right) \tag{25}$$

However, this equation is based on the pore pressure at the midface of the cone, which is rarely measured, except in some research projects, but the pore pressure at the shaft is usually available. The relation between both excess pore pressures can be expressed as:

$$(u_1 - u_0) = \beta(u_2 - u_0) \tag{26}$$

Previous field research (Peuchen et al. 2010) in addition to numerical simulations (Monforte et al. 2021,2023a) have shown that for normally consolidated or slightly over-consolidated soils typical values of β range between 1.2 to 1.4.

Thus, using this last expression, Equation (24) can be rewritten as:

$$\frac{q_t - \beta(u_2 - u_0) - u_0}{p_0'} = c_q \left(1 + \frac{2M}{3}\right) \exp\left(-\frac{\psi_0}{\lambda}\right) \tag{27}$$

To quantify the validity of the hypotheses assumed to propose the expression of the geometric correction factor, c_q, Equation (25) can be rearranged as:

$$q_t - u_1 = c_q \left(1 + \frac{2M}{3}\right)\left(\frac{2}{M}\right) \left[p_0' \frac{M}{2} \exp\left(-\frac{\psi_0}{\lambda}\right)\right] \tag{28}$$

in which the last bracketed term corresponds to the critical state undrained shear strength, see Equation (7). Therefore, this last equation defines an approximation to the bearing capacity factor as:

$$N_{ke1}^{res} = \frac{q_t - u_1}{S_u^{res}} = c_q \left(1 + \frac{2M}{3}\right)\left(\frac{2}{M}\right) \tag{29}$$

where S_u^{res} stands for the critical state undrained shear strength. Evaluating this cone factor for $M = 1$ yields cone factors ranging as: $3.33 < N_{ke1}^{res} < 4.33$, whereas for $M = 1.33$ it can be shown that $2.84 < N_{ke1}^{res} < 3.84$. (Moreover, the numerical simulations also show this decrease of N_{ke1}^{res} as M increases.) In the numerical simulations reported in this work, Figure 10, this cone factor falls well within the range, implying that the assumed hypotheses hold to a large extent.

3.4.2. Comparison with previous expressions

Validation of state parameter inversion techniques against calibration chamber databases is unfeasible, as no such test has been performed in which the cone response is undrained. Therefore, some attempts to validate CPTu interpretation techniques by comparing outputs of these techniques to the state parameter obtained from element testing on high quality samples have found an overall qualitative agreement (Shuttle & Cunning 2007; Shuttle & Jefferies 2016), but not quantitative. These differences have been attributed in a large extend to sampling disturbance -particularly uncertainty of the as-recovered void ratio- (Shuttle & Jefferies 2016); and the hypothesis underlying the interpretation technique as a minor contributory factor (Shuttle & Cunning, 2007). The validation of CPTu interpretation techniques based on elementary testing of recovered soil samples seems therefore to be a Sisyphean task.

Table 2. CPTu in undrained, liquefiable materials. Expressions of the normalized effective tip resistance and fitting parameters.

$$Q' = \overline{k}\exp(-\overline{m}\psi_0)$$

	Normalized effective tip resistance, Q'	Fitting parameter $\overline{k}$	Fitting parameter $\overline{m}$
Plewes (Jefferies and Been 2015)	$\frac{q_t - u_2}{p'_0}$	$M\left(3 + \frac{0.37}{\lambda}\right)$	$11.9 - 30.62\lambda$
Pezeshki and Ahmadi (2022)	$\frac{q_t - p_0}{p'_0}\left(1 - \frac{u_2 - u_0}{q_t - \sigma_{v0}}\right) + 1$	$M\left(3.3 - \frac{0.035}{\lambda}\right)$	$6 + \frac{0.1735}{\lambda}$
Mo et al. (2024)	$\frac{q_t - u_2}{p'_0} \approx \frac{q_t - u_2}{\sigma'_{v0}}$	$\left(1 + \frac{2M}{3}\right)(1 + \tan(\delta))$	$\frac{1}{\lambda}$
This work	$\frac{q_t - \beta(u_2 - u_0) - u_0}{p'_0}$	$c_q\left(1 + \frac{2M}{3}\right)$	$\frac{1}{\lambda}$

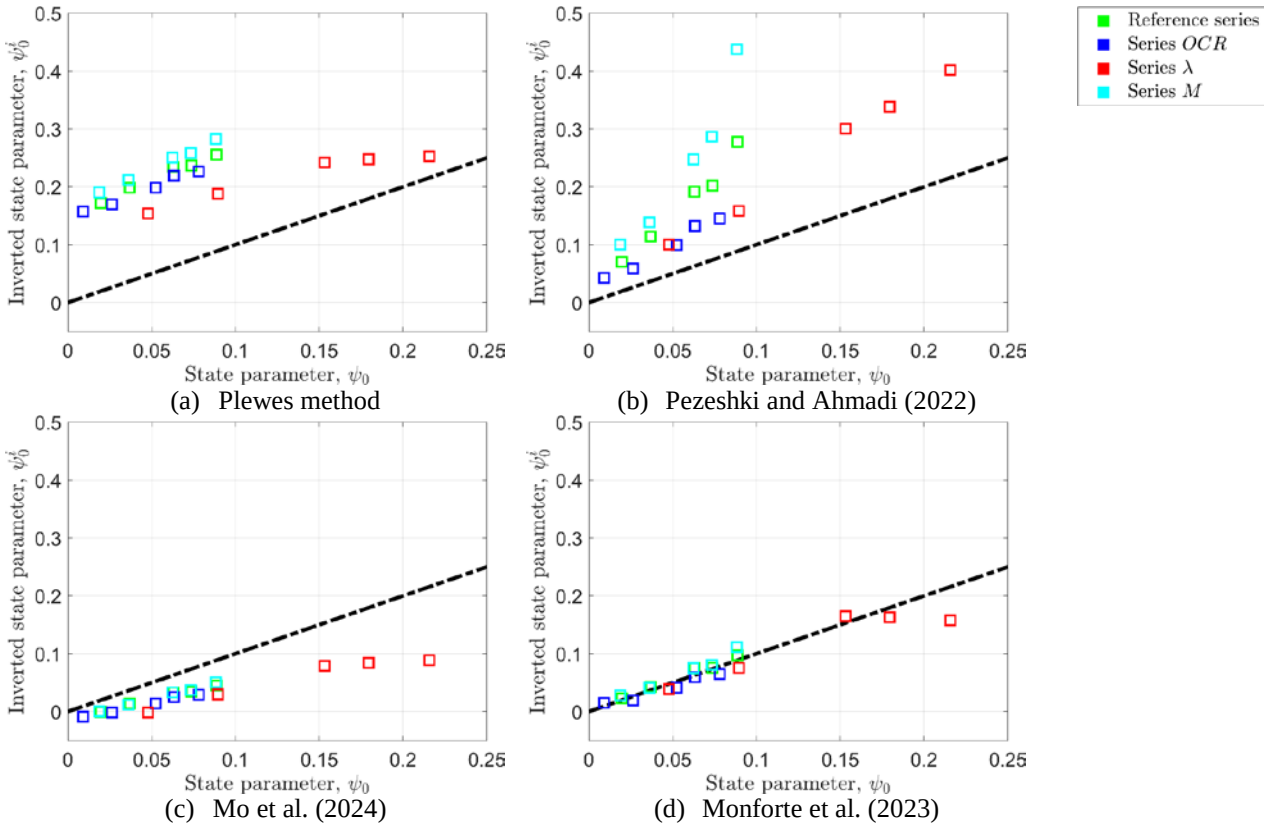

Figure 11. CPTu in undrained, liquefiable materials. Initial state parameter of the simulation and interpreted state parameter using different techniques.

Other works (Monforte et al. 2024) have attempted to infer the reliability of each of interpretation technique by means of other rationales, namely comparing these interpretation techniques to current empirical knowledge commonly used to interpret the CPTu in undrained conditions.

A thorough validation is not sought in this work. In this document, the presented numerical results are used to assess the performance of the proposed interpretation technique in addition to the screening method of Plewes (Plewes et al. 1992; Jefferies and Been 2015) and the recently developed by Pezehski and Ahmadi (2022). The expression of the fitting parameters, $\overline{k}$ and $\overline{m}$, in addition to the definition of the normalized effective tip resistance, which is slightly different for each method, are reported in Table 2.

Plewes screening method (Jefferies and Been 2015) seems to consistently over-predict the state parameter. Moreover, it is worth noting that all simulations performed considering soils with a small, near zero, initial state parameter plot in current practice CPTu interpretation charts in the region of soft, normally consolidated, insensitive clays. Instead, for these simulations, Plewes method predicts state parameters ranging from 0.1 to 0.2.

The technique proposed by Pezeshki and Ahmadi (2022) seems to adequately predict the state parameter for simulations with the lowest state parameter (even with some scatter), but overestimates the state parameter

as higher state parameters are considered. Not only that, but the technique seems to work better for larger values of the plastic compressibility, λ, than for smaller ones and better for $M = 1$ and worse for $M = 1.3$.

The proposal of Mo et al. (2024) is biased and consistently underpredicts the state parameter. This proposal (which shares some common traits with that developed in this work) is based on cavity expansion results. Differently from the one proposed here, that considers two scaling terms, the proposal of Mo et al. (2024) only considers one scaling term between the effective cone tip resistance, $q_t - u_2$, and the effective cavity resistance, $\sigma_c - u_c$, to tackle the frictional behavior of the cone-soil interface: that is $q_t - u_2 \approx (\sigma_c - u_c)\,(1 + \tan(\delta))$, being δ the soil-interface friction angle. The biased behavior of this technique can be attributed to the consideration of the u_2 water pressure as an analogue of the cavity water pressure, u_c. It has long been recognized (Shuttle and Jefferies 2016) that the water pressure during the expansion of a cavity corresponds to the excess pore pressure at the mid-face of the cone, u_1, and one additional scaling term is required to go from $u_c \approx u_1$ to u_2.

The interpretation technique proposed in this work seems to be the one that performs better. One could argue that this is just confirmation bias, as the same numerical results have been used both to inspire the proposed interpretation technique and for its validation. However, a number of arguments can be provided to support the proposed state parameter inversion technique. First, all bearing capacity factors, and especially those related to the residual undrained shear strength, are well in the range of current empirical knowledge on the interpretation of CPTu in fine grained, sensitive materials; the state parameter and the undrained shear strength are intimately related to each other, see Equation (7). Secondly, the tendencies observed on normalized cone metrics as the state parameter increases are as expected. Finally, the hypotheses that have been used to propose the technique are reasonable. A more thorough comparison and discussion of state parameter inversion techniques are reported elsewhere (Monforte et al. 2024).

4. Soil disturbance due to tube sampling

Tube sampling is commonly used to obtain specimens of soft soils. The process encompasses several processes which might produce disturbance in the recovered soil sample, namely boring, sampling, storage, extrusion and the early stages of testing. In any case, the sampler geometry (thickness, shape of the cutting shoe, inside clearance) and the sampling technique play a prominent role in the disturbance caused to the sample. Therefore, the reduction of strength, stiffness and preconsolidation stress observed in samples will depend on the employed tube and sampling technique when compared to block samples (Hvorslev 1949; Hight 2003; Ladd and DeGroot 2003).

Most of the knowledge on sampling disturbance has been gathered by experimental field work and subsequent laboratory testing (Hvorslev 1949). Periodically, this knowledge has been summarized to provide practical advice (La Rochelle et al. 1981; Lunne et al. 1997; Clayton & Siddique 1999). In soft clays, disturbance is minimized by employing very thin, beveled, smooth sampling tubes. Also, the use of a stationary piston is recommended. These recommendations are similar to those already suggested by Hvorslev (1949).

The most influential theoretical approach to describe sampling disturbance is the so-called 'Ideal Sampling Approach' (Baligh et al. 1987). The theory is based on the Strain Path Method (SPM) (Baligh 1985). SPM assumes that the strain path caused by the insertion of a rigid object into a soil mass is independent of the constitutive response of the soil; moreover, the deformation path of the soil corresponds to that obtained in a flow around the tube sampler by an ideal fluid (Baligh 1985).

These analyses show that the strain path at the central part of the soil that enters the tube is quite homogeneous. For this reason, it is assumed that the vertical straining history at the centerline of the tube can be used to infer the disturbance caused to the soil sample (Baligh et al. 1987). This theory predicts that for round-tipped tubes the vertical strain at the centerline is inversely related to the thickness of the tube (Baligh et al 1987). Moreover, SPM can also be used to quantify the reduction of the vertical strain at the centerline of the soil in a tube using beveled cutting shoes (Clayton et al. 1998; Clayton and Siddique 1999).

Despite the general acceptance of the 'Ideal Sampling Approach' among the geotechnical community, this approach has been occasionally questioned. For instance, Santagata et al. (2006) tested several samples of a reconstituted soil obtained with different samplers and found that the disturbance caused to the sample (in terms of undrained shear strength and yield stress) is much higher than obtained by applying the strain path predicted to the 'Ideal Sampling Approach' in an unaltered sample. In addition, the physical modelling of Hover et al (2013) shows that the centerline strain path obtained in a transparent, undrained soil is not in agreement with the one predicted by the Strain Path Method.

Apart from the SPM, most research efforts to understand the effect of the geometry of the tube on the sample disturbance have been conducted either by field testing or physical modelling, extracting samples with different tubes and subsequently testing them in the laboratory to obtain the reduction of undrained strength or yield stress; this is expensive, time consuming and subject to uncertainty derived from uncontrolled factors, such as the inherent soil variability. Despite the relevance of sampling disturbance for geotechnical practice, few numerical efforts have been conducted to investigate this problem.

The objective of this section is to present two sets of numerical simulations aimed at characterizing the effect of the geometry of the tube on the recovered sample in fine grained materials. In both sets of simulations, it is assumed that the insertion of sampling tubes is an undrained process. The first set of simulations (Monforte et al. 2022a, b) is carried out as a total stress analysis, in which the response of the soil is modelled with an elasto-perfectly plastic Tresca model, and aims to characterize the kinematics of tube insertion and discuss the similitudes and differences of the numerical results with

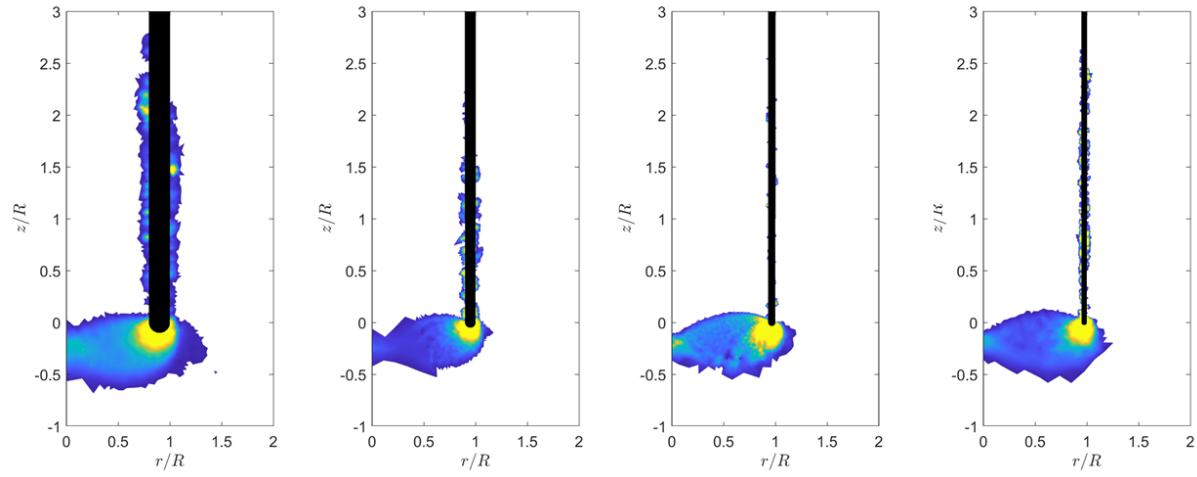

Figure 12. Tube insertion. Total stress analysis. Round-tipped sampler. Incremental plastic shear strain for different tube thicknesses.

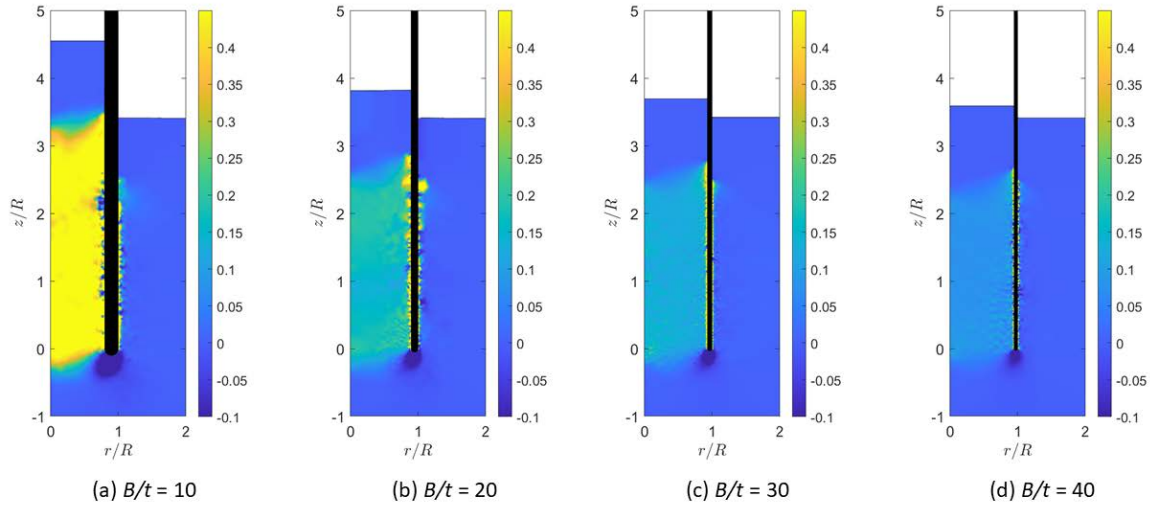

Figure 13. Tube insertion. Total stress analysis. Round-tipped sampler. Vertical unit elongation for different tube thicknesses.

the predictions of the Strain Path Method. In the second set we employ a fully coupled hydromechanical formulation and describe the response of the soil with a critical state constitutive model that accounts for structure and destructuration. In this case, we quantify the effect of the tube geometry on the degree of disturbance produced in two relevant design parameters: the peak undrained shear strength and the yield stress. This is done by simulating undrained triaxial tests and oedometer tests on the material that has entered the tube, in close connection with Hvorslev (1949) methodology.

Here, we focus on the effect of the thickness of the tube for round-tipped samplers and samplers with a beveled cutting shoe (20º). We do not consider the effect of placing a stationary piston inside of the piston nor the effect of the bevel angle of the cutting shoe different from 20º. The effect of other beveled cutting shoes, of the presence of a stationary piston and their combined effect in total stress analysis is presented elsewhere (Monforte et al, 2022).

4.1. Total stress analyses

The first set of simulations corresponds to the total stress analysis of tube sampling. The constitutive response of the soil is modelled with an elastic perfectly plastic model. In particular, the elastic part is described with a linear, quasi-incompressible elastic model relating the Hencky elastic strain and the Kirchoff stress and, for the plastic componenet, a Tresca yield surface is employed. In the simulations presented here, the rigidity index is equal to $I_r = \frac{G}{S_u} = 100$, G being the shear modulus and $S_u = 10$ kPa the undrained shear strength. Simulations employing other rigidity indices are reported elsewhere (Monforte 2018), showing no influence of the rigidity index on the numerical results.

Due to the symmetry of the problem, the tube insertion is simulated using an axisymmetric model. At the vertical boundaries, null radial displacements are prescribed, whereas null displacements are set at the

bottom boundary. At the upper free surfaces, a load of 200 kPa is prescribed. The initial stress state of the soil is set to a total mean stress of 200 kPa and null deviatoric stress; cases with initial anisotropic stress states are presented in Monforte (2018), showing no effect on the deformation path of the problem. In these simulations, the effect of the initial weight of the soil is neglected.

The tube is initially wished in place at some depth. The tube is assumed smooth, representative of a well-maintained tube.

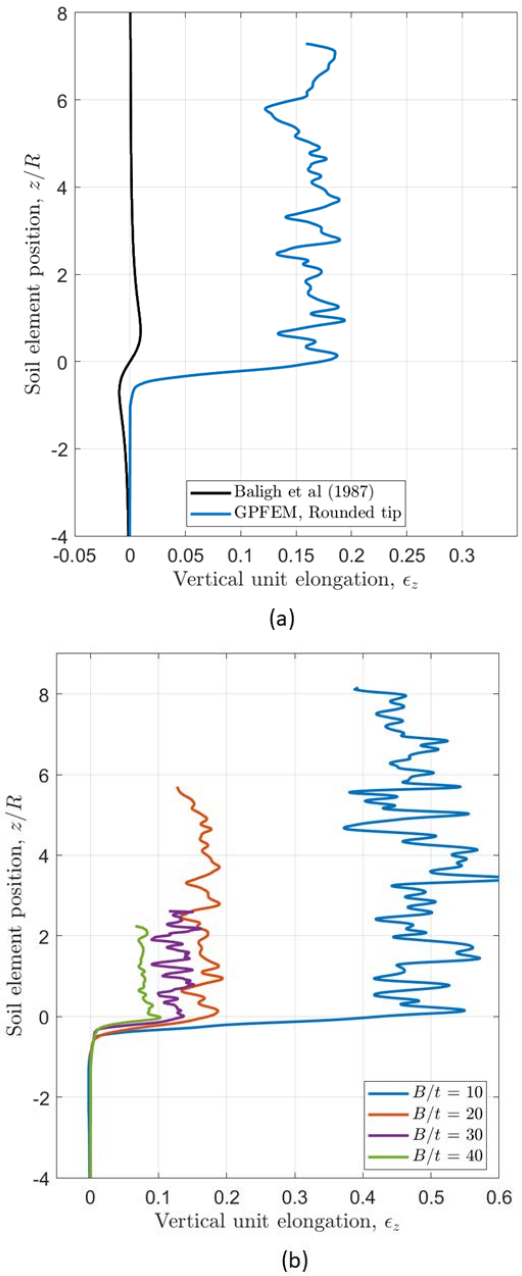

Figure 14. Tube insertion. Total stress analysis. Round-tipped sampler. Centreline straining path. Comparison of the Strain Path method (Baligh et al. 1987) and PFEM simulations for *B/t* = 20, (a). Numerical results for different sampler thicknesses, (b).

4.1.1. Round-tipped sampler

Figure 12 and Figure 13 present the numerical results of tube insertion for several tube thicknesses, characterized by the ratio B/t, where B is the outer diameter of the tube and t the thickness of the tube. For the thicknesses considered here, ranging from $B/t = 10$ to 40, the same failure mechanism prevails, as evidenced by the incremental plastic multiplier, whose contour plot is independent of the thickness of the tube. From the cutting shoe of the tube to the axis of symmetry of the problem, there is a region of high plastic straining, whereas the rest of the soil mass remains in elastic regime, except for some small regions inside the tube, which are caused by numerical noise. As the tube is inserted, it creates a plastic failure mechanism in which most of the soil that lies beneath the tube (including the tip of the tube) gets squeezed inside the tube. Once inside the tube, the soil remains in the elastic regime. Not all material that is initially beneath the tip of the tube enters the tube, but part of it gets diverted into the far field, as indicated by the plastic strains.

The contour plots of the vertical strain of these four simulations are a consequence of this failure mechanism. Vertical strains are small almost everywhere, with the exception of the material that enters the tube (Figure 13). As the tube advances, the material first suffers from small compression vertical straining, but as it gets nearer the entrance of the tube, it gets squeezed into the tube, leading to high vertical extension strains. The magnitude of the maximum extension vertical strain reduces as the ratio between the outer diameter of the tube and its thickness (B/t) increases.

In all simulations, an excess of sample is recovered, that is, the length of the recovered sample is larger than the advance of the tube. This excess of recovered material also reduces as the ratio between the outer diameter of the tube and its thickness (B/t) increases and it is a consequence of the prevailing strain path and failure mechanism.

As customary in the 'Ideal Sampling Approach', Figure 14 reports the centerline vertical strains predicted by GPFEM and those from the Strain Path method (Baligh et al. 1987). It is evident that both approaches predict strain paths that are not quantitatively nor qualitatively in agreement. Qualitatively, SPM predicts that the extension vertical strains progressively tend to zero as the soil travels inside the tube; instead, in the PFEM simulations, straining at the entry of the tube is irrecoverable and, once inside the tube, strains hardly vary. Quantitatively, PFEM extension vertical strains are almost one order of magnitude larger than those predicted by SPM, whereas the compression ones are one order of magnitude smaller.

A variety of arguments can be put forward to explain the huge discrepancies between the predictions of both methods.

First and foremost, the assumed constitutive response of soil: elasto-plasticity in PFEM and a perfect fluid in SPM. PFEM simulations show a clear failure mechanism in which plastic irrecoverable straining takes place. Instead, SPM makes no distinction between recoverable and irreversible strains.

Secondly, the assumed boundary conditions. In SPM the domain is considered infinite, and null displacements are prescribed there; one of the consequences is that the whole soil domain has a downwards displacement (see Sagaseta et al. 1997 or Monforte et al. 2022). These boundary conditions prevent an excess of material from

entering the sampler (contrary to what is observed in PFEM simulations in Figure 13). Thus, these boundary conditions control -or contribute to control- the predicted strain path. In contrast, in PFEM, the domain has a finite dimension, and a vertical load is placed at the upper boundary. Therefore, the strain path and the amount of material that enters the sampler are affected by these boundary conditions (that are thought of as more realistic) and by the constitutive response of the soil.

Third, and probably the least important cause, is the geometry of the tube. Initially, SPM relied on analytical solutions to estimate the flow around rigid objects. As such, the predictions of the strain path method do not consider tube with straight shafts, but with slightly curved ones. In PFEM simulations, shafts are completely straight and vertical.

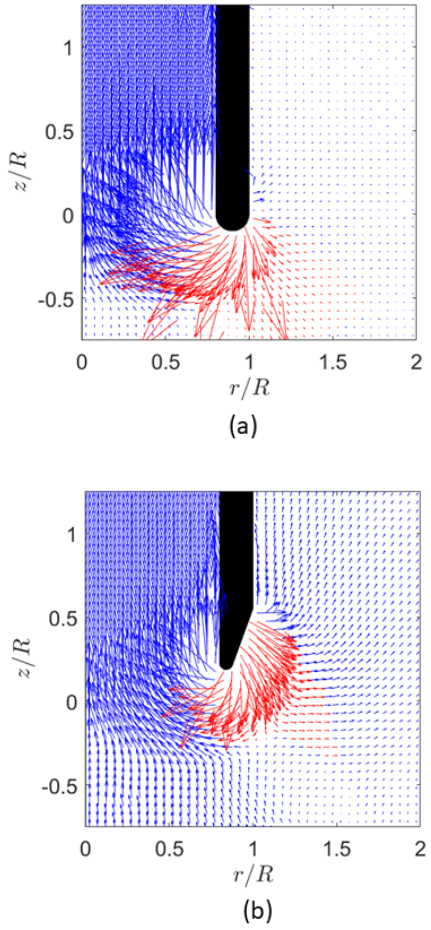

Figure 15. Tube insertion. Total stress analysis. Comparison of the velocity field during tube insertion for a round-tipped tube, (a), and one with a bevelled cutting shoe, (b). B/t = 10.

4.1.2. Beveled tube

Additional numerical simulations have been performed to assess the effect of a beveled cutting shoe, with an angle of 20º. The plastic failure mechanism (not reported here) has similitudes with that obtained in the round-tipped case: plasticity takes place at the entry of the tube. However, the ratio between the volume of soil that enters the tube to the volume of soil displaced into the far field is affected by the shape of the cutting shoe of the tube. This is demonstrated in 0, showing the velocity field for two samplers of identical thickness but different tip geometry. In the round tipped case, the amount of soil that is diverted into the far field is far smaller than for the beveled cutting shoe.

As a consequence of the slightly different failure mechanism, in which the amount of soil that is diverted into the far field is different, the strain path of the problem also presents some differences: by beveling the cutting shoe of the tube, the vertical strains of the material that enter the tube are reduced (see Figure 16).

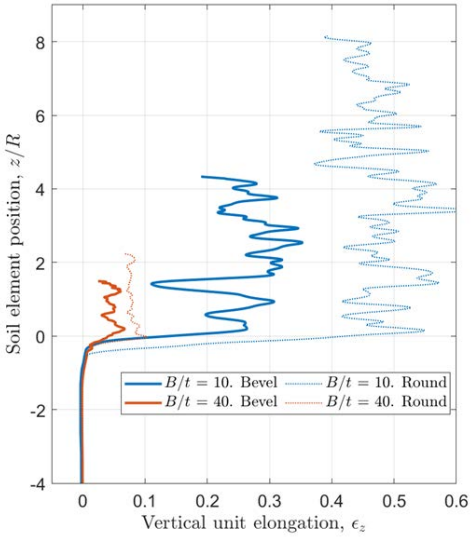

Figure 16. Tube insertion. Total stress analysis. Centreline straining path for different cutting shoe geometries and different thickness of the tube.

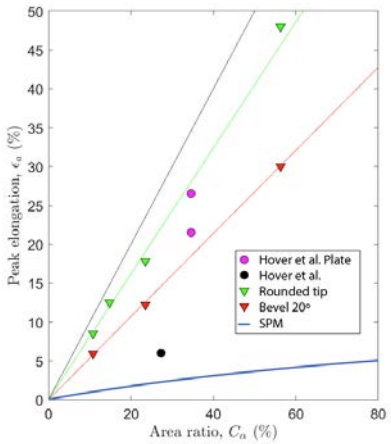

Figure 17. Tube insertion. Total stress analysis. Maximum vertical extension unit elongation in terms of the area ratio of the tube.

4.1.3. Discussion: Hvorslev fraction

Figure 17 reports the peak extension vertical strain at the centerline of the problem in terms of the area ratio of the tube, defined as the ratio of the area of the tube (structure) to the internal area of the tube (i.e. the area occupied by the sampled soil). Numerical results show a linear dependency between the area ratio of the tube and the peak vertical extension strain at the centerline.This figure also reports results of the physical modelling of tube sampling on transparent soil of Hover et al (2013), using a round-tipped tube. These results are in qualitative

agreement with those reported here, obtained using PFEM. Neither the physical modelling results (Hover et al. 2013) nor the numerical modelling results show the same tendencies as the prevailing theoretical results of the 'Ideal Sampling Approach'.

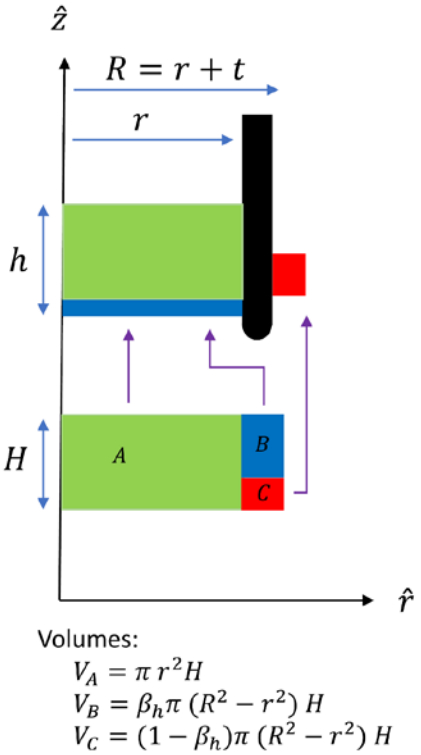

Figure 18. Graphical representation of the Hvorslev fraction and the proposed rationale to interpret the maximum vertical elongation.

In Monforte et al (2022) we introduced the Hvorslev fraction to analyze these numerical results. This metric is inspired by the previously described failure mechanism, i.e. the diversion of the volume of soil that lies beneath the tube as the tube penetrates. For undrained sampling, the volume of the sampler must be accommodated by displacing soil and that displaced soil will partly enter the tube, increasing by the amount of soil strictly beneath the sampler mouth.

As sketched in Figure 18, the extra material that is diverted inside of the tube, V_b, is expressed as a ratio of the volume of material that lies just beneath the tube, $V_b + V_c$, leading to the definition of the Hvorslev fraction as:

$$\beta_H = \frac{V_b}{V_b + V_c} \tag{30}$$

Assuming undrained conditions, the vertical deformation can be expressed as:

$$\epsilon_z = \frac{h-H}{H} = \frac{\beta_H \pi (R^2 - r^2) + \pi r^2}{\pi r^2} - 1 = \beta_h C_\alpha \tag{31}$$

where $C_\alpha = \frac{R^2 - r^2}{r^2}$ stands for the area ratio of the tube, with $R = D/2$ and $r = R - t$ as the outer and inner radii of the tube.

Interestingly, the numerical results reported here suggest that -at least in the range of tube area ratios reported here- the Hvorslev fraction is independent of the thickness of the tube. In other words, the Hvorslev fraction of a round-tipped sampler without a stationary piston inside of the sampler is around 0.81 whereas that of a beveled tube is 0.53. Further parametric analyses considering other tube geometries suggest that the Hvorslev fraction only depends on the cutting shoe geometry and the presence or absence of a stationary piston inside of the tube (Monforte et al 2022a,b). It is worth noting that this is the case for the considered range of thicknesses of the tubes (from $B/t = 10$ to $B/t = 40$) in undrained conditions and considering a highly idealized constitutive response of the soil (i.e. unsensitive clays).

4.2. Coupled hydromechanical analyses

The previous analyses was used to describe the kinematic response of the soil during tube sampling, but no information on the disturbance of the soil within the sampler (other than the maximum extension vertical strain in the centerline of the problem) has been obtained. In order to quantify the effect of sampling on important parameters of the soil (namely the undrained shear strength and the yield stress) we have performed a second set of analyses. In this case, the porous media is described using a fully coupled hydromechanical formulation and the constitutive response of the soil is modelled using a critical state constitutive model that considers the effect of structure (bonding) and its loss due to plastic straining.

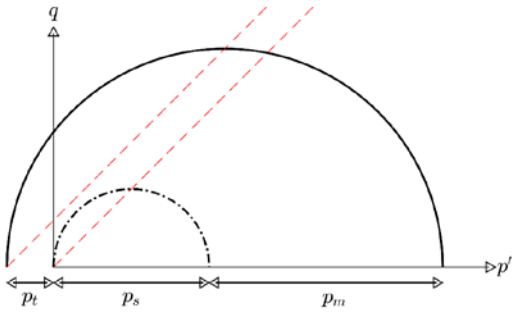

Figure 19. Sketch of the yield surface in the $p' - q$ plane for triaxial conditions.

4.2.1. Constitutive model and adopted material parameters

A broad number of constitutive models able to realistically reproduce soil destructuration have been proposed (Gens and Nova 1993; Liu and Carter 2002). Some of them consider anisotropy effects (Korskinen et al. 2002; Wheeler et al. 2003; Karstunen et al. 2005), chemical coupling (Ciantia and di Prisco 2016) or even stiffness degradation with strain by employing elements of bounding surface plasticity (Rouainia and Muir Wood 2000). In the analyses reported herein, a modified version of CASM (Yu 1998) extended to account for structure and destructuration is used (Gens and Nova 1993; González 2011). Therefore, the yield surface is expressed as:

$$f = \left(\frac{q}{M_\theta (p' + p_t)}\right)^n + \frac{1}{\ln(r)} \ln\left(\frac{p' + p_t}{p_t + p_s + p_m}\right) \tag{32}$$

where p' and $q = \sqrt{3 J_2}$ are invariants of the Kirchoff effective stress tensor. M_θ is the stress ratio at critical

state, which varies on Lode's angle according to a smoothed Mohr-Coulomb failure criterion (Abbo et al. 2011).

The model has three stress-like hardening variables, graphically depicted in Figure 19. p_s stands for the preconsolidation stress of the reference, unstructured soil, whereas p_t and p_m stand for the increase in the yield stress along isotropic paths in tensile and compressive loading, respectively. These variables representing structure are proportional to the reference preconsolidation stress through the bonding variable, b (Gens and Nova 1993):

$$p_m = b\, p_s \tag{33}$$

$$p_t = \alpha\, b\, p_s \tag{34}$$

where α is a soil constitutive parameter and the bonding variable, b, evolves according to:

$$b = b_0 \exp\left(-(h - h_0)\right) \tag{35}$$

where b_0 is the initial value of the bonding variable. The strain-like variable h evolves with volumetric and deviatoric plastic strains:

$$\mathrm{d}h = h_1 \left|\mathrm{tr}\, \boldsymbol{l}^p\right| + h_2 \sqrt{\tfrac{2}{3}}\, l_d^p \tag{36}$$

where h_1 and h_2 are two constitutive parameters representing the rate of degradation in terms of volumetric and deviatoric plastic strains, $\boldsymbol{l}^p$ is the spatial plastic velocity gradient and $l_d^p = \sqrt{\mathrm{dev}(\boldsymbol{l}^p) : \mathrm{dev}(\boldsymbol{l}^p)}$.

The reference preconsolidation stress follows a classical isotropic hardening rule of critical state soil mechanics. A non-associated flow rule is adopted. A suitable stress integration technique, with integral-type non-local regularization, is used (Monforte et al. 2019).

As the aim of this section is to assess the disturbance caused by tube sampling, four different sets of constitutive parameters are employed, which differ in terms of the initial bonding, ranging from $b_0 = 0.2$ to $b_0 = 3$. That is, all four materials have the same initial reference preconsolidation stress, while each material has a different value of p_t and p_m, thus a different amount of structure. The adopted constitutive parameters are $\lambda = 0.2$, $\kappa = 0.016$, $M = 1$, $p_s = 250$ kPa, $n = 1.5$, $r = 2$, $h_1 = 7.5$, $h_2 = 2.3$, $\alpha = 0.2$.These parameters are characteristic of a broad class of structured clays (González et al. 2009; González 2012), where the case with the lowest structure represents a soft, normally consolidated clay with a slight structure.

To illustrate the constitutive response of these four materials, Figure 20 and Figure 21 report two laboratory tests: undrained triaxial testing and oedometric loading. In all cases, the initial stress state corresponds to an effective vertical stress of 200 kPa and a $K_0 = 0.65$, which coincides with the initial stress state of the boundary value problems that are reported below.

The effective stress path and deviatoric stress-axial deformation in undrained (compression and extension) triaxial loading for the four sets of parameters are reported in Figure 20. Once the stress path touches the yield surface, plastic strains start to develop and the bonding variable, b, and the stress-like hardening variables p_t and p_m tend to zero, leading to a strain-softening response of the material. All four materials share the same residual undrained shear strength, but the peak undrained shear strength increases with the initial bonding.

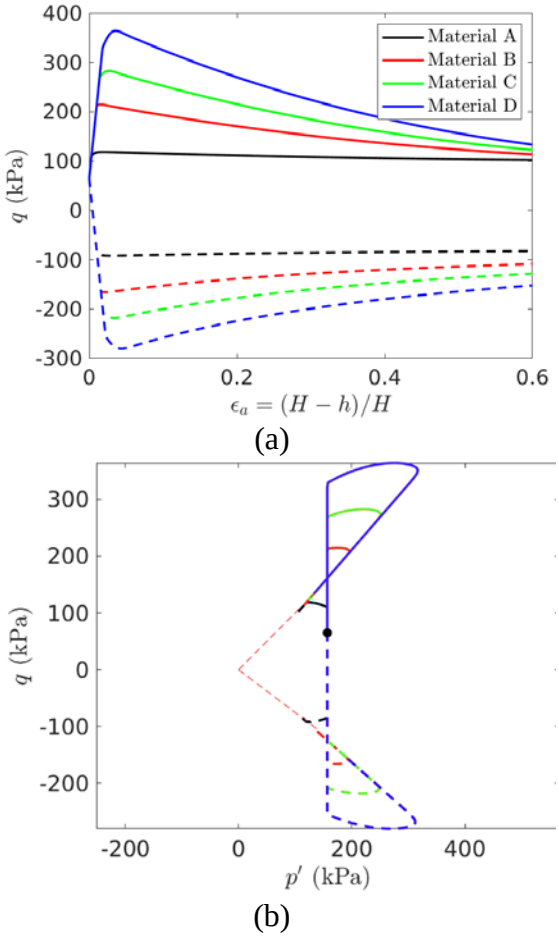

Figure 20. Tube insertion. Coupled hydromechanical analysis. Undrained compression and extension triaxial tests: evolution of deviatoric stress in terms of the axial deformation, (a), and stress path in the $p' - q$ plane, (b). Continuous lines: triaxial compression. Dashed lines: triaxial extension.

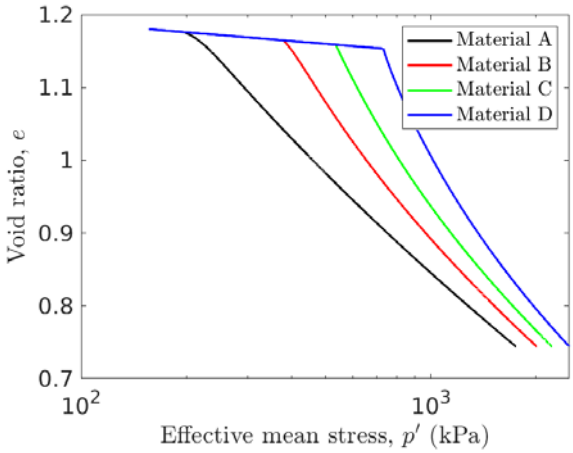

Figure 21. Tube insertion. Coupled hydromechanical analysis. Oedometric loading. Evolution of the void ratio in terms of the effective mean stress.

The isotropic response is shown in Figure 21, reporting the evolution of void ratio with effective mean stress. As all materials share the same initial value of p_0

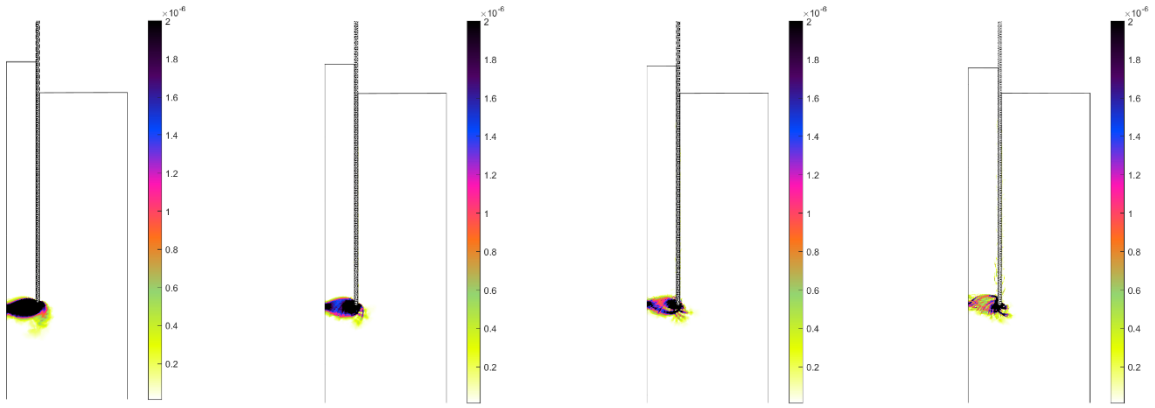

(a) Material A (b) Material B (c) Material C (d) Material D

Figure 22. Tube insertion. Coupled hydromechanical analysis. Round-tipped sampler, D/t = 20. Incremental plastic shear strain for materials A, B, C and D.

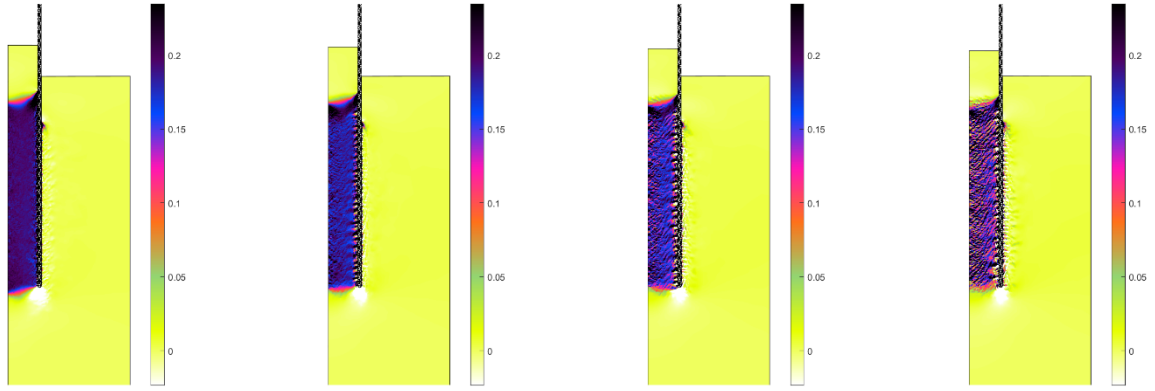

(a) Material A (b) Material B (c) Material C (d) Material D

Figure 23. Tube insertion. Coupled hydromechanical analysis. Round-tipped sampler, B/t = 20. Vertical deformation for materials A, B, C and D.

but not the initial bonding, materials with a larger value of b yield at higher stresses. As the material is further loaded, destructuration takes place and the void ratio tends to the reference compression line of the unstructured material.

4.2.2. Kinematics of tube sampling in structured materials

The geometry and boundary conditions of the numerical model are quite similar to the one employed in the previous section. In this case, since a coupled hydromechanical formulation is employed, null excess pore pressure is prescribed at the top and bottom boundaries. A low value of permeability has been used, so practically undrained conditions prevail during the simulation. As before, the tube is considered fully smooth.

The first set of simulations correspond to a thick, round-tipped sampler with a diameter-to-wall thickness ratio of $B/t = 20$ (Monforte et al, 2023c). Tube sampling has been simulated for the four materials with different brittleness. Figure 22 reports the incremental plastic shear strain after a tube insertion of 2.5 diameters. The limited area of soil experiencing plastic flow extends from the cutting shoe to the axis of symmetry of the problem; the rest of the soil mass remains in the elastic regime. Moreover, the shape of the active plastic zone seems independent of the brittleness of the soil and is coincident with the one obtained in the previous section.

The vertical deformation of the soil is a consequence of the plastic failure mechanism: as the tube advances, the soil that lies below the tube experiences vertical extension and compression in the two horizontal directions (i.e. triaxial extension conditions) until it enters the tube. Thus, vertical strains are large and almost

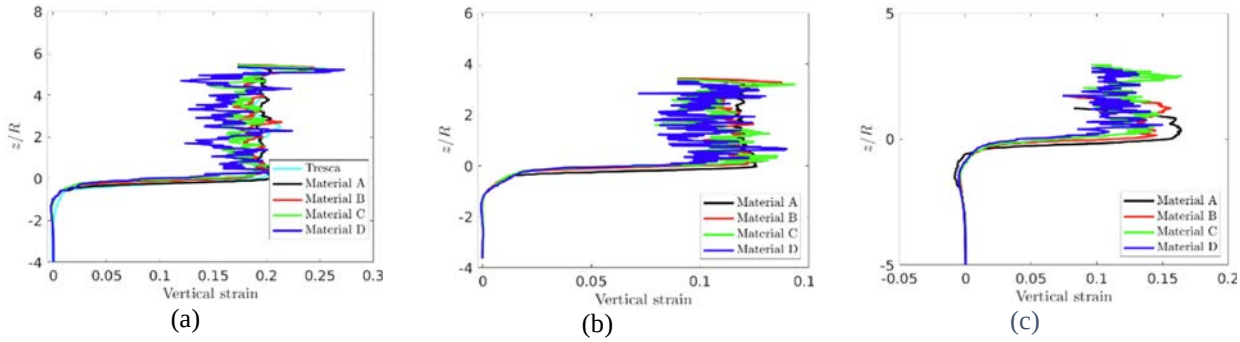

Figure 24. Tube insertion. Coupled hydromechanical analysis. Centerline strain path for round-tipped samplers: B/t = 20, (a), B/t = 30, (b). Centerline for a beveled cutting shoe and B/t = 20, (c).

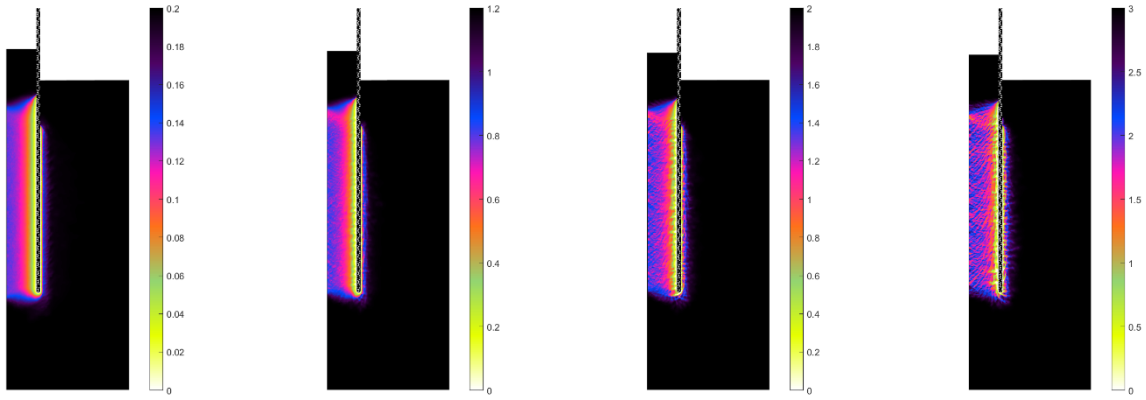

(a) Material A (b) Material B (c) Material C (d) Material D

Figure 25. Tube insertion. Coupled hydromechanical analysis. Round-tipped sampler. B/t = 20. Bonding variable for materials A, B, C and D.

homogeneous inside of the tube (except at the upper part, since the tube is initially assumed wished in place at a depth of 1R) and below the cutting shoe of the tube and small elsewhere. The value of the vertical strain inside of the tube is approximately 20%, slightly decreasing as larger values of initial bonding are considered (see Figure 23).

The centerline strain path, the vertical deformation at the axis of symmetry of the problem, is a consequence of this failure mechanism, see Figure 24. The obtained kinematic response of the soil during tube sampling shows little influence of the initial bonding, suggesting that the deformation of the soil is controlled by the kinematic restriction of the problem. Indeed, the deformation path is in good agreement with previous analyses of tube sampling of insensitive, undrained clays modelled using a total stress approach (see the previous subsection).

To characterize the effect of sampling on the stress and hardening variables of the soil, Figure 25 reports the spatial distribution of the current available bonding for the four materials. As expected from the plastic failure mechanism, bonding decreases within the material that enters the tube and along the outer shaft of the tube. For the most brittle material, the bonding variable shows some oscillations in the vertical direction, as the material exhibits some mild tendency to localize. In the radial direction, a larger decrease of the bonding variable is observed next to the inner shaft with respect to the centerline. This is because the soil that lies near the inner shaft, first experience some plastic vertical compression as the cutting shoe of the tube approaches the soil element and then vertical extension as it enters the tube. In contrast, the soil at the centerline of the tube only experiences plastic vertical extension straining.

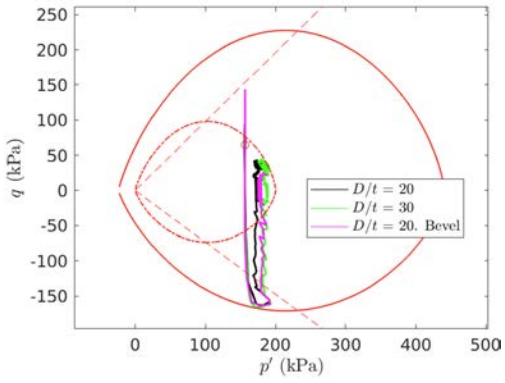

Figure 26. : Tube insertion. Coupled hydromechanical analysis. Material B. Stress path followed by a point located at the centerline of the problem for different tube geometries.

The evolution of the stress path of a soil element located at the centerline of the problem is depicted in Figure 26 for the case $b_0 = 1.2$. As the tube approaches

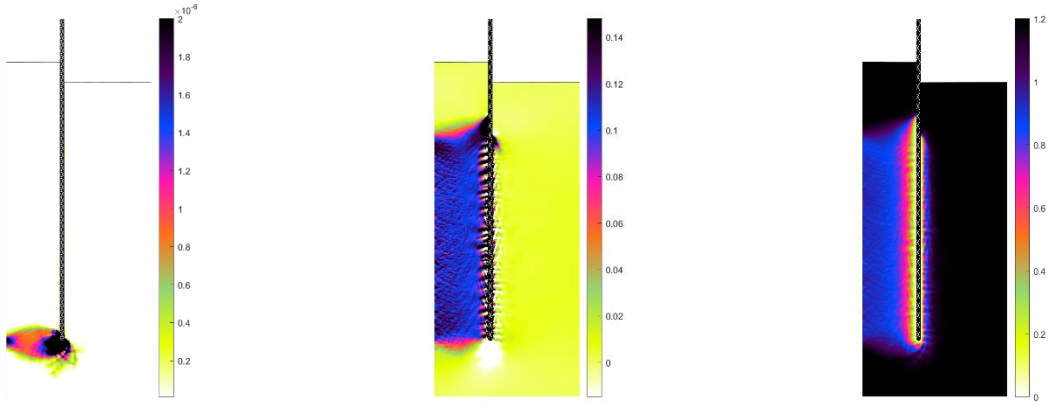

(a) (b) (c)

Figure 27. Tube insertion. Coupled hydromechanical analysis. Round tipped sampler. D/t = 30. Material B. Incremental plastic multiplier, (a), vertical deformation, (b), and bonding variable, (c).

the soil element, it induces triaxial compression strains; the magnitude of which is small (see Figure 26) and, hence, results in elastic straining. The soil element experiences large triaxial extension strains as it enters the tube, which causes elastic straining first and then plastic flow; in the elasto-plastic regime, the available bonding reduces from $b_0 = 1.2$ to $b \approx 0.6$ as the soil element enters the tube. Once the soil element has entered the tube, deviatoric stresses tend to zero elastically at constant effective mean stress (undrained conditions).

The thickness of the tube has long been recognized as one of the key parameters influencing sampling disturbance (Hvorslev, 1949). To assess the effect of this parameter on the results, the insertion of a tube with $B/t = 30$ in the four considered materials has been simulated. Numerical results confirm that the same failure mechanism than for the thicker tube prevails, see Figure 27, that shows the incremental plastic multiplier for the case b_0 = 1.2. The magnitude of the extension vertical strain inside of the tube reduces with respect to the thicker tube and is of the order of 15%.

As a consequence of this reduction of the strain level, the soil that enters the tube suffers less destructuration. The stress path of a representative soil element located in the axis of symmetry of the problem is shown in Figure 26. Again, results show the same tendencies as for the thick tube; however, the magnitude of the induced deviatoric strains, both in compression and extension, are slightly lower, reducing the amount of destructuration during tube insertion.

Four additional simulations have been performed, considering a beveled cutting shoe (20º) and a diameter to thickness ratio of *B/t* = 20. The strain path and the failure mechanism (not reported here due to a matter of space) are almost coincident with those obtained using a total stress approach for an elastic perfectly plastic material. Consequently, and compared to the results using the same thickness but a round-tipped cutting shoe, beveling the cutting shoe of the tube produces a lower decrease of the bonding variable of the material that enters the tube.

Again, the outputs of the simulations are plotted in terms of the area ratio of the tube vs the Hvorslev fraction (see Figure 28). Importantly, numerical results show that the Hvorslev fraction in undrained tube sampling is independent of the material constitutive response (i.e. the brittleness of the material) and of the area ratio of the tube and only depends on the geometry of the cutting shoe.

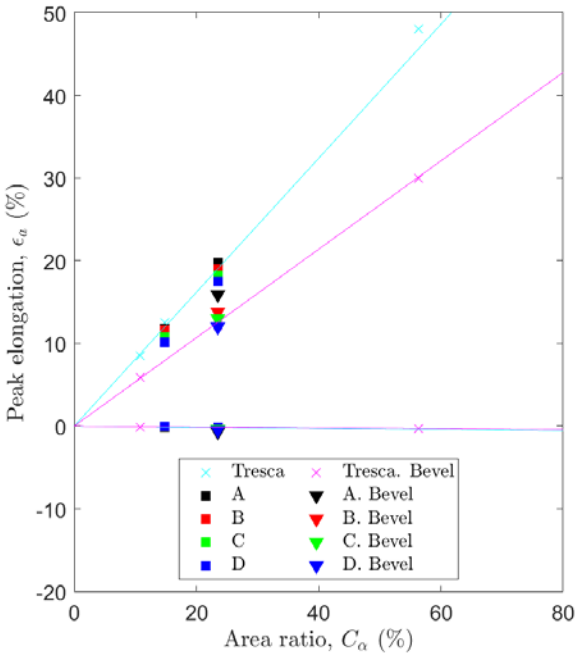

Figure 28. Tube insertion. Coupled hydromechanical analysis. Peak vertical elongation in terms of the geometry of the cutting shoe and area ratio of the tube.

4.2.3. Quantification of sampling disturbance

Sampling disturbance may be further characterized by its effect on key soil parameters employed in design, such as the variation of peak undrained shear strength or the yield stress.

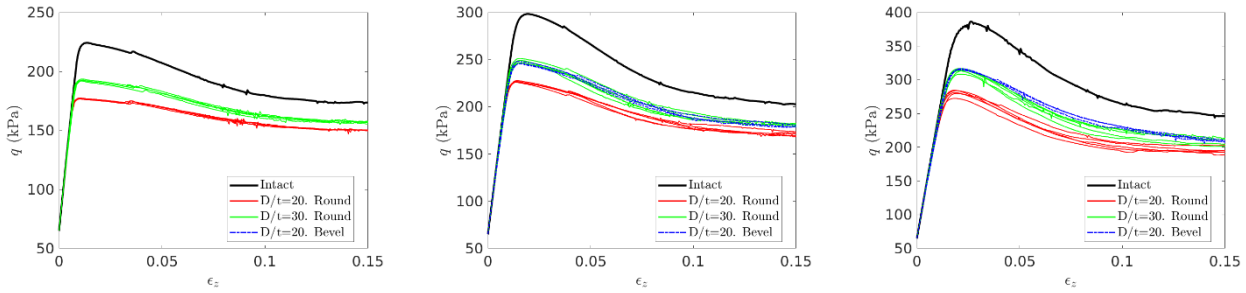

(a) Material B (b) Material C (c) Material D

Figure 29. Tube insertion. Coupled hydromechanical analysis. Quantification of sampling disturbance. Undrained triaxial loading on material inside of the tube: Material B, (a), Material C, (b), and Material D, (c).

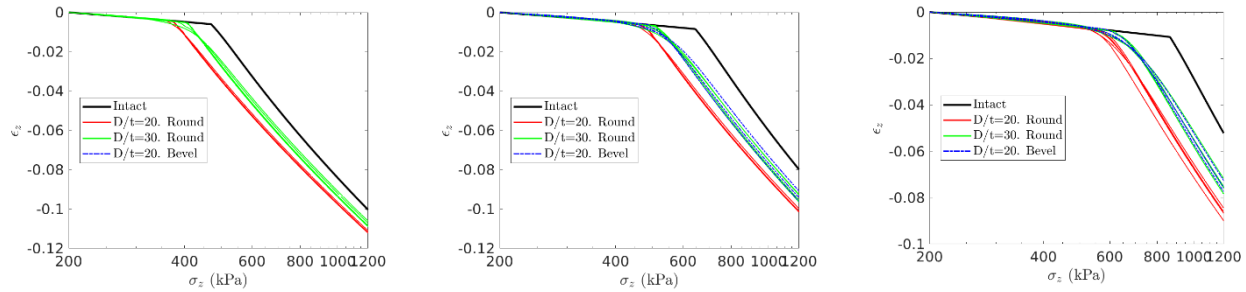

(a) Material B (b) Material C (c) Material D

Figure 30. Tube insertion. Coupled hydromechanical analysis. Quantification of sampling disturbance. Oedometric loading on material inside of the tube: Material B, (a), Material C, (b), and Material D, (c).

In this work, a methodology inspired by the empirical methodology used by Hvorslev (1949) is employed: tube insertion is numerically simulated and a laboratory test is computed in material that has entered the tube. It ought to be said that this numerical approach only quantifies the sample disturbance due to tube insertion; other sources of disturbance (sampler extraction, transportation, storage sample preparation,….) frequently found relevant (Ladd and DeGroot 2004) are disregarded.

Two types of laboratory tests, frequently employed to characterize sampling disturbance, are considered: (i) unconsolidated K_0 compression triaxial loading and (ii) oedometric loading. In both cases, the radius of the tested sample is one third of the radius of the outer radius of the tube; for the oedometric loading the height of the sample is equal to the radius whereas, for the triaxial loading, the height is twice the radius of the sample. In both cases, the information of the material inside of the tube (elastic and plastic variables, water pressure, ...) is transferred into a new, finer finite element mesh to compute the boundary value problem simulating the laboratory test.

For the unconsolidated triaxial test, the stress path is as follows: after transferring the stress state to the new finite element mesh, vertical and horizontal loads of 200 and 135 kPa, respectively, are prescribed without allowing for any excess pore pressure equalization. Afterwards, axial deformation is prescribed, assuming that both the top and bottom plates are fully rough. To simulate the oedometric test, the soil is first allowed to consolidate at a vertical stress of 200 kPa and null radial displacement. After excess pore pressure equalization, axial deformation is prescribed.

As previously mentioned, the state of the soil inside the tube is not homogeneous, especially in the simulations in which strain localization is present. Thus, to assess the effect of the variability of the soil, five different computations are performed for each material and sampler geometry, which differ in its location inside the tube at the end of the tube insertion simulation.

Figure 29 reports the main output of interest for the triaxial loading for the four materials: the evolution of the deviatoric stress in terms of axial strain. The first thing to note is that the variability among each computation is limited even though some of the computations show a slightly different shear banding.

Results of the undrained triaxial loading on all materials share similar traits. On the one hand, for each material (i) the peak undrained shear strength decreases with increasing area ratio of the tube and (ii) a beveled cutting shoe in a tube with B/t = 20 leads to a similar peak undrained shear strength that a tube with B/t = 30 with a round-tipped shoe. This can be explained by the different degree of destructuration induced by each sampler geometry: thinner tubes reduce the amount of destructuration as well as beveling the cutting shoe. On the other hand, soil disturbance is more pronounced as the material has more structure: the undrained shear strength reduces by 14% for a tube of B/t = 30 in material B; in contrast, for the most brittle material it reduces by 20%.

Similar conclusions can be drawn from the results of the simulation of the oedometer tests, Figure 30. Thicker tubes produce higher destructuration of the soil during sampling and, thus, the soil yields at lower stress levels.

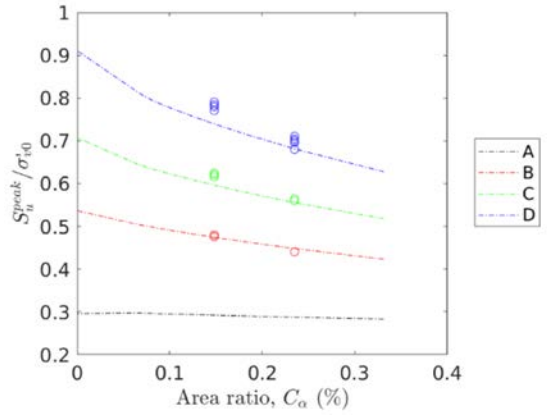

(a) Round tipped tube. Triaxial loading.

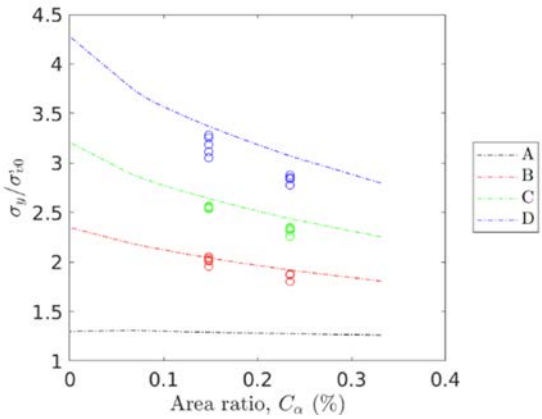

(b) Round tipped tube. Oedometric loading.

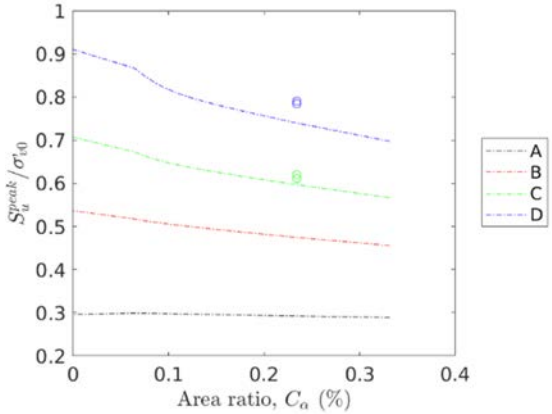

(c) Beveled tube. Triaxial loading

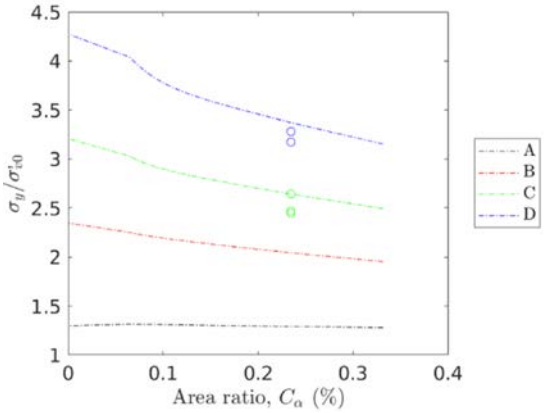

(d) Beveled tube. Oedometric loading.

Figure 31. Tube insertion. Coupled hydromechanical analysis. Degradation of the yield stress and peak undrained shear strength in terms of the area ratio of the tube for round-tipped tubes, (a) and (b), and beveled cutting shoes (c) and (d). Results depicted with a circle correspond to those obtained in a boundary value simulation whereas those with a discontinuous line correspond to the Gauss point analysis.

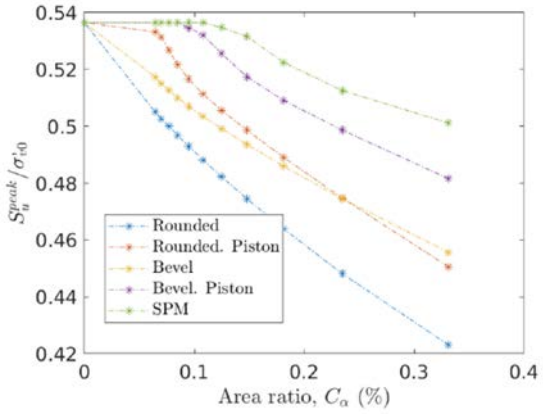

(a)

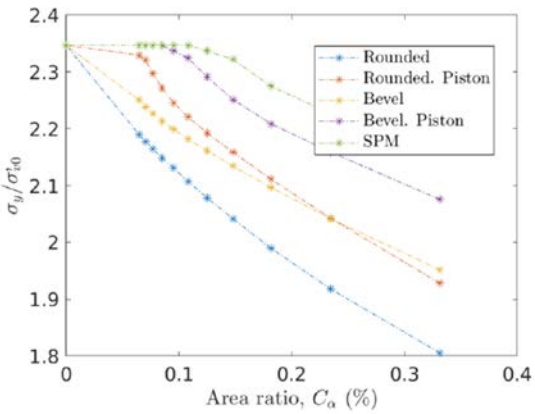

(b)

Figure 32. Tube insertion. Coupled hydromechanical analysis. Degradation of the peak undrained shear strength, (a), and the yield stress, (b), for several cutting shoe geometries and area ratios of the tube. Material B.

Sampling disturbance is also associated with stiffness degradation (Siddique et al. 2000). However, the numerical results presented here show the same stiffness during the first phase of triaxial loading or one-dimensional compression; this is because the soil behaves elastically and elastic stiffness degradation due to previous loading has not been considered in the constitutive model.

4.2.4. Discussion

The model based on the Hvorslev fraction may be employed to infer soil disturbance based on the strain history but, more importantly, to assess the effect of sampling on key geotechnical soil constitutive parameters, such as the peak undrained shear strength or the preconsolidation stress. To this end, a new series of simulations has been performed in which a single Gauss point is first subject to the relevant compression and

extension strains in undrained triaxial conditions (extension predicted by Equation (31); compression by a similar expression in Monforte et al. 2022a), brought back to the initial stress state (K_0 conditions) and, finally, the desired loading path (oedometer test or undrained triaxial compression test) is computed.

Figure 31 reports the main results of interest of this analysis, the peak undrained shear strength and the yield stress, in terms of the area ratio of the tube for the four materials. The peak shear strength and the yield stress decrease as larger area ratios are considered, since tube sampling produces a larger destructuration during the penetration of the soil. The degradation of these variables also depends on the brittleness of the material, as these variables reduce at a faster rate for more brittle materials. Of course, for the least brittle material (almost insensitive), disturbance due to sampling is almost negligible, as prior plastic flow produces very limited destructuration, see Figure 25. It ought to be said that for very small area ratios, Equation (31) predicts small strains, which result in elastic loading, thus sampling does not produce destructuration. Further research to investigate the validity of Equation (31) for very thin samplers is therefore needed.

Figure 31 also reports the peak undrained shear strength and yield stress obtained in the previous subsection, computing a boundary value problem. Importantly, a remarkable agreement is found between both methods to predict sampling disturbance.

Assuming that the Hvorslev fraction is constant and independent of the area ratio of the tube and based on the good agreement between both methods to infer disturbance (the integration of a strain path in a Gauss point and the simulation of tube sampling and then the laboratory test), curves of variation of undrained shear strength and yield stress may be tentatively traced for a variety of sampler geometries (Figure 32). These curves are in close agreement with empirical knowledge in the field: sampling disturbance is alleviated using tubes with a low area ratio, employing beveled cutting shoes and the presence of a stationary piston to prevent the formation of a heave.

For completeness, the same rationale has been employed this time prescribing the strain path predicted by the Strain Path method (Baligh et al. 1987) for a round-tipped tube. Degradation of the undrained shear strength and yield stress is much lower compared to the predictions based on PFEM simulations, as SPM predicts lower peak strains induced by tube insertion. This result would explain why experimental programs that mimicked the centerline strain path in a triaxial cell prior to one-dimensional loading of the soil found out that the 'Ideal Sampling Approach' tests tends to show less disturbance compared to real samples retrieved from a tube (Santagata et al, 2006).

5. Conclusions

With the advance of numerical methods, it is now possible to numerically simulate several insertion problems which are particularly relevant for geotechnical site characterization. These numerical simulations give new insights on the processes that take place during the insertion of the rigid structure into soil masses, which can be used to challenge current empirical interpretation methods used in practice or even propose new ones based on numerical analyses.

This work has explored two long-standing problems in geotechnical engineering: the interpretation of the cone penetration test and the soil disturbance due to tube sampling.

Numerical modelling has given new insights on the stress state around a cone penetrating an undrained, liquefiable soil. These new insights have been used to propose a new interpretation technique for the inversion of the state parameter from cone metrics, based on an analytical solution of cavity expansion modified to tackle the geometric mismatch between cone penetration and cavity expansion.

The second set of numerical analyses explored the mechanisms by which the soil enters the tube during tube sampling. Full details of the prevailing strain path and plastic failure mechanism has been given, in addition to the effect of the geometry of the tube on them. Furthermore, hydro-mechanical simulations of tube sampling on undrained, structured soil have been used to quantify the disturbance of the insertion on important design parameters of the soil.

Although a number of assumptions have been made (e.g. undrained behavior, isotropic constitutive model…) in both set of analyses, the numerical computations have been able to capture the essential features of the problem and provide valuable insights. Moreover, the two sets of analyses reported here have shed light on two specific problems and have demonstrated that new insights into classical geotechnical problems can still be gained by advanced numerical modelling. It is envisaged that numerical modelling will play a prominent role in further developments in the field of site characterization, by progressively replacing empirical knowledge with that gathered by simulation. That seems to be a real promise of advanced numerical techniques.

Acknowledgements

The authors express their sincere gratitude and appreciation to Prof. Josep Maria Carbonell (CIMNE/Universitat de Vic) for his invaluable collaboration in all the numerical developments leading to this research.

Thanks are extended to Dr Laurin Hauser (CIMNE), Dr Stefano Collico (DMT), Diego Durán (CIMNE), David León (UPC), Dr Dani Tarragó (CIMNE), Davide Besenzon (ESPOL), Prof M. Rouainia, Dr Abdallah Najdi, Gosai Alyamani (Newcastle University) and Dr Katia Boschi (Politecnico di Milano) for many fruitful discussions and advice.

The authors gratefully acknowledge financial support of Ministerio de Ciencia, Innovación y Universidades of Spain (MCIN/AEI/10.13039/501100011033) through the Severo Ochoa Centre of Excellence project (CEX2018-000797-S) and research project PID2020-119598RB-I00.

References

Abbo, A.J., Sloan, S.W. “A smooth hyperbolic approximation to the Mohr-Coulomb yield criterion”, Computers and Structures, 54(3), pp. 427-441, 1995. http://doi.org/10.1016/0045-7949(94)00339-5

Abbo, A.J., Lyamin, A.V., Sloan, S.W., Hambleton, J.P. “A C2 continuous approximation to the Mohr-Coulomb yield surface”, International Journal of Solids and Structures, 48(21), pp. 3001-3010, 2011. https://doi.org/10.1016/j.ijsolstr.2011.06.021

Ansari, Y., Merifield, R., Sheng, D. “A piezocone dissipation test interpretation method for hydraulic conductivity of soft clays”, Soil and Foundations, 54(6), pp. 1104-1116, 2014. https://doi.org/10.1016/j.sandf.2014.11.006

Arroyo, M., Butlanska, J., Gens, A., Calvetti, F., Jamiolkowski, M. “Cone penetration tests in a virtual calibration chamber”, Géotechnique, 61(6), pp. 525-531, 2011. https://doi.org/10.1680/geot.9.P.067

Baligh, M.M. “Strain Path method”, Journal of Geotechnical Engineering, 111(9), pp. 1108-1136, 1985. https://doi.org/10.1061/(ASCE)0733-9410(1985)111:9(1108)

Baligh, M.M., Azzouz, A.S., Chin, C.-T., “Disturbances due to the ‘ideal’ tube sampling”, Journal of Geotechnical Engineering, 113(7), pp. 739-757, 1987. https://doi.org/10.1061/(ASCE)0733-9410(1987)113:7(739)

Bažant, Z.P., Jirásek, M. “Nonlocal integral formulation of plasticity and damage: survey of progress”, Journal of Engineering Mechanics, 128(11), pp. 1119-1149, 2002. https://doi.org/10.1061/(ASCE)0733-9399(2002)128:11(1119)

Been, K., Jefferies, M.G. “A state parameter for sands”, Géotechnique, 35(2), pp. 99-112, 1985. https://doi.org/10.1680/geot.1985.35.2.99

Bochev, P.B., Dohrmann, C.R., Gunzburger, M.D. “Stabilization of low-order mixed finite elements for the Stokes equations”, SIAM Journal on Numerical Analysis, 44(1), pp. 82-101, 2006. https://doi.org/10.1137/S0036142905444482

Boschi, K., Arroyo, M., Monforte, L., Carbonell, J.M., Gens, A. “Coupled hydromechanical modelling of cone penetration in layered liquefiable soils”, Géotechnique, ahead of print, 2024. https://doi.org/10.1680/jgeot.23.00164

Butlanska, J., Arroyo, M., Gens, A. OSullivan, C. “Multi-scale analysis of cone penetration (CPT) in a virtual calibration chamber”, Canadian Geotechnical Journal, 51(1), pp. 51-66. 2014. https://doi.org/10.1139/cgj-2012-0476

Carbonell, J.M., Oñate, E., Suárez, B. “Modeling of ground excavation with the particle finite-element method”, Journal of Engineering Mechanics, 136(4), pp. 455–463, 2010. https://doi.org/10.1061/(ASCE)EM.1943-7889.0000086

Carbonell, J.M., Oñate, E., Suárez, B “Modelling of tunnelling processes and rock cutting tool wear with the particle finite element method”, Computational Mechanics, 52(3), pp. 607–629. 2013. https://doi.org/10.1007/s00466-013-0835-x

Carbonell, J.M., Monforte, L., Ciantia, M.O., Arroyo, M., Gens, A. “Geotechnical particle finite element method for modeling of soil-structure interaction under large deformation conditions”, Journal of Rock Mechanics and Geotechnical Engineering, 14(3), pp. 967-983, 2022, https://doi.org/10.1016/j.jrmge.2021.12.006

Carter, J.P., Booker, J.R., Yeung, S.K. “Cavity expansion in cohesive frictional soils”, Géotechnique, 36(3), pp. 349-358, 1986. https://doi.org/10.1680/geot.1986.36.3.349

Ceccato, F., Beuth, L., Simonini, P. “Analysis of piezocone penetration under different drainage conditions with the two-phase material point method”, Journal of Geotechnical and Geoenvironmental Engineering, 142(12), 04016066, 2016. https://doi.org/10.1061/(ASCE)GT.1943-5606.0001550

Ciantia, M.O., di Prisco, C. “Extension of plasticity theory to debonding, grain dissolution, and chemical damage of calcarenites”, International Journal for Numerical and Analytical Methods in Geomechanics, 40(3), pp. 315-343, 2016. https://doi.org/10.1002/nag.2397

Ciantia, M.O., Arroyo, M., Butlanska, J., Gens, A. “DEM modelling of cone penetration tests in a double-porosity crushable granular material”, Computers and Geotechnics, 73, pp. 109-127, 2016. https://doi.org/10.1016/j.compgeo.2015.12.001

Clayton, C.R.I., Siddique, A. “Tube sampling disturbance – forgotten truths and new perspectives”, Proceedings of the Institution of Civil Engineers – Geotechnical Engineering, 137(3), pp. 127-135, 1999. https://doi.org/10.1680/gt.1999.370302

Clayton, C.R.I., Siddique, A., Hopper, R.J. “Effects of sampler design on tube sampling disturbance – numerical and analytical investigations”, Géotechnique, 48(6), pp. 847-867, 1998. https://doi.org/10.1680/geot.1998.48.6.847

Cundall, P.A., Strack, O.D.L “A discrete numerical model for granular assemblies”, Géotechnique, 29(1), pp. 47-65, 1979. https://doi.org/10.1680/geot.1979.29.1.47

Davies, M.P., McRoberts, E., Martin, T. “Static liquefaction of tailings – fundamentals and case histories”. In: Tailing Dams, Las Vegas, USA, 2002.

De Borst, A., Vermeer, P.A. “Possibilities and limitations of finite elements for limit analysis”, Géotechnique, 32(2), pp. 199-210, 1984. https://doi.org/10.1680/geot.1984.34.2.199

Edelsbrunner, H., Mücke, E.P. “Three-dimensional alpha shapes” ACM Transaction of Graphics, 13(1), pp. 43-72, 2003. https://doi.org/10.1145/174462.156635

Fourie, A., Verdugo, R., Bjelkevik, M., Torres-Cruz, L.A., Znidarcic, D. “Geotechnics of mine tailings: A 2022 state of the art”. In: 20th International Conference on Soil Mechanics and Geotechnical Engineering. Sidney, Australia, 2022.

Gens, A., Nova, R. “Conceptual bases for a constitutive model for bonded soils and weak rocks”. In: International Symposium on Geomechanical Engineering of Hard Soils and Soft Rocks, pp. 485-494, 1993.

Galavi, V., Schweiger, H.F. “Nonlocal multilaminate model for strain softening analysis”, International Journal of Geomechanics, 10(1), pp. 30-44, 2010. http://doi.org/10.1061/(ASCE)1532-3641(2010)10:1(30)

González, N.A. “Development of a family of constitutive models for geotechnical applications”, PhD Thesis, Universitat Politècnica de Catalunya, 2011.

González, N.A., Rouainia, M., Arroyo, M., Gens, A. “Analysis of tunnel excavation in London Clay incorporating soil structure”, Géotechnique, 62(12), pp. 1095-1109, 2012. https://doi.org/10.1680/geot.11.P.030

Hauser, L., Schweiger, H.F. “Numerical study on undrained cone penetration in structured soil using G-PFEM”, Computers and Geotechnics, 133, 104061, 2021. https://doi.org/10.1016/j.compgeo.2021.104061

Hauser, L., Schweiger, H.F. “Numerische Simulation von Drucksondierungen mithilfe der Particle Finite Element Method”, Bautechnik, 100(9), pp. 535-543, 2023. https://doi.org/10.1002/bate.202300053

Hight, D.W., “Sampling effects in soft clay: an update on Ladd and Lambe (1963)”. In: Soil Behavior and Soft Ground Construction: Proceedings of the Sympisoum on Soil Behavior and Soft Ground Construction honoring Charles C. ‘Chuck’ Ladd, pp. 86-121, 2003.

Hover, E.D., Ni, Q., Guymer, I. “Investigation of centreline strain path during tube penetration using transparent soil and particle image velocimetry”. Géotechnique Letters. 3(2), pp. 37–41, 2013. https://doi.org/10.1680/geolett.13.00017

Hu, Y., Randolph, M.F. “A practical numerical approach for large deformation problems in soils”, International Journal for Numerical and Analytical Methods in Geomechanics, 22(5), pp. 327-350, 1998. https://doi.org/10.1002/(SICI)1096-9853(199805)22:5%3C327::AID-NAG920%3E3.0.CO;2-X

Hvorslev, M.K. “Subsurface exploration and sampling of soils for civil engineering purposes Report on a research project of the Committee on Sampling and Testing, Soil Mechanics and Foundations Division, American Society of Civil Engineers”, Vicksburg, USA, 1949.

Idelsohn, S.R., Oñate, E., del Pin, F. “The particle finite element method: a powerful tool to solve incompressible flows with free-surfaces and breaking waves”, International Journal for Numerical Methods in Engineering, 61(7), pp. 964-989, 2004. https://doi.org/10.1002/nme.1096

Jefferies, M., Been, K. “Soil liquefaction: a critical state approach, second edition”, CRC Press, London, United Kingdom, 2015. https://doi.org/10.1201/b19114

Karlsrud, K., Lunne, T., Kort, D.A., Strandvikk, S. “CPTU correlations for clays” In: Proceedings of the 16th International Conference on Soil Mechanics and Geotechnical Engineering, pp. 693-702, 2005.

Karstunen, M., Krenn, H., Wheeler, S.J., Koskinen, M., Zentar, R. “Effect of anisotropy and destructuration on the behavior of Murro test Embankment”, International Journal of Geomechanics, 5(2), pp. 87- 87, 2005. https://doi.org/10.1061/(ASCE)1532-3641(2005)5:2(87)

Khosravi, A., Martinez, A., DeJong, J.T. “Discrete element model (DEM) simulations of cone penetration test (CPT) measurements and soil classification” Canadian Geotechnical Journal, 57(9), pp. 1369-1387, 2020. https://doi.org/10.1139/cgj-2019-0512

Koskinen, M., Karstunen, M., Wheeler, S.J. “Modelling destructuration and anisotropy of a natural soft clay”. In: Proceedings of the 5th European Conference on Numerical Methods in Geotechnical Engineering, pp. 11-20, 2002.

La Rochelle, P., Sarrailh, J., Tavenas, F., Roy, M., Leroueil, S. “Causes of sampling disturbance and design of a new sampler for sensitive soils”, Canadian Geotechnical Journal, 8(1), pp. 52-66, 1981. https://doi.org/10.1139/t81-006

Ladd, C.C., De Groot, D.J.” Recommended practice for soft ground site characterization: Arthur Casagrande lecture”. In: Proceedings of the 12th Pan-American Conference on Soil Mechanics and Geotechnical Engineering, 2003.

Liu, M.D., Carter, J.P. “A structured Cam Clay model”, Canadian Geotechnical Journal, 39(6), pp. 1313-1332, 2002. https://doi.org/10.1139/t02-069

Lobo-Guerrero, S. Vallejo, L. E. “DEM analysis of crushing around driven piles in granular materials”, Géotechnique, 55(8), pp. 617-623, 2005. http://dx.doi.org/10.1680/geot.2005.55.8.617

Lu, Q., Randolph, M.F., Hu, Y., Bugarski, I.C. “A numerical study of cone penetration in clay”, Géotechnique, 54(4), pp. 257-267. 2004. http://doi.org/10.1680/geot.2004.54.4.257

Lunne, T., Berre, T., Strandvik, S. “Sample disturbance effects in soft low plasticity Norwegian clay”, In: Recent Developments in Soil and Pavement Mechanics, pp. 81-102, 1997.

Mánica, M.A., Gens, A., Vaunat, J., Ruiz, D.F. “Nonlocal plasticity modelling of strain localization in stiff clays”, Computers and Geotechnics, 103, pp. 138-150, 2018. https://doi.org/10.1016/j.compgeo.2018.07.008

Mánica, M.A., Arroyo, M., and Gens, A. 2021. “Effects of tailings viscosity on liquefaction triggering analyses”. In: Tailings and Mine Waste conference, Alberta, Canada, 2021.

Mánica, M.A., Arroyo, M., Gens, A., Monforte, L. 2022. “Application of a critical state model to the Merriespruit tailings dam failure”. Proceedings of the Institution of Civil Engineers – Geotechnical Engineering, 175(2), pp. 151-165, 2022. https://doi.org/10.1680/jgeen.21.00001

Martinelli, M., Galavi, V. “Investigation of the material point method in the simulation of cone penetration tests in dry sand”, Computers and Geotechnics, 130, 103923, 2021. https://doi.org/10.1016/j.compgeo.2020.103923

Martinelli, M., Pisanò, F. “Relating cone penetration resistance to sand state using the material point method”, Géotechnique Letters, 12(2), pp. 131-138, 2022. https://doi.org/10.1680/jgele.21.00145

Mo, P.Q., Yu, H.S. “Undrained cavity expansion analysis with a unified state parameter model for clay and sand”, Géotechnique, 72(1), pp. 61-77, 2017. https://doi.org/10.1680/jgeot.15.P.261

Mo, P.-Q., Cai, G., Wang, K.-J., Eslami, A., Yu, H.S. “Cavity expansion-based interpretation of piezocone penetration test (CPTu) data in clays”, Géotechnique, ahead of print, 2024. https://doi.org/10.1680/jgeot.23.00045

Monforte, L., Arroyo, M., Gens, A., Carbonell, J.M. “Explicit finite deformation stress integration of the elasto-plastic constitutive equations”, In: Computer Methods and Recent Advances in Geomechanics – Proceedings of the 14th International IACMAG conference, Kyoto, Japan, pp. 267-272, 2014.

Monforte, L., Arroyo, M., Carbonell, J.M., Gens, A. “Numerical simulation of undrained insertion problems in geotechnical engineering with the Particle Finite Element Method (PFEM)”, Computers and Geotechnics, 82, pp. 144-156, 2017a. https://doi.org/10.1016/j.compgeo.2016.08.013

Monforte, L., Carbonell, J.M., Arroyo, M., Gens, A. “Performance of mixed formulations for the particle finite element method in soil mechanics problems”, Computational Particle Mechanics, 4, pp. 269-284, 2017b. https://doi.org/10.1007/s40571-016-0145-0

Monforte, L. “Insertion problems in geomechanics with the particle finite element method”, PhD Thesis, Universitat Politècnica de Catalunya, 2018. http://dx.doi.org/10.5821/dissertation-2117-124709

Monforte, L., Arroyo, M., Carbonell, J.M., Gens, A. “Coupled effective stress analysis of insertion problems in geotechnics with the Particle Finite Element Method”, Computers and Geotechnics, 101, pp. 114-129, 2018a. https://doi.org/10.1016/j.compgeo.2018.04.002

Monforte, L., Arroyo, M., Gens, A., Carbonell, J.M. “Hydraulic conductivity from piezocone on-the-fly: a numerical evaluation”, Géotechnique Letters, 8(4), pp. 268-277, 2018b. https://doi.org/10.1680/jgele.18.00108

Monforte, L., Ciantia, M.O., Carbonell, J.M., Arroyo, M., Gens, A. “A stable mesh-independent approach for numerical modelling of structured soils at large strains”, Computers and Geotechnics, 116, pp. 103215, 2019. https://doi.org/10.1016/j.compgeo.2019.103215

Monforte, L., Gens, A., Arroyo, M., Mánica, M., Carbonell, J.M., “Analysis of cone penetration in brittle liquefiable soils”, Computers and Geotechnics, 134, 104123, 2021. https://doi.org/10.1016/j.compgeo.2021.104123

Monforte, L., Arroyo, M., Carbonell, J.M., Gens, A. “Large-strain analysis of undrained smooth tube sampling”, Géotechnique, 72(1), pp. 61-77, 2022a. http://dx.doi.org/10.1680/jgeot.19.p.354

Monforte, L., Arroyo, M., Gens, A., Carbonell, J.M. “A new approach to evaluate the soil disturbance due to tube sampling”; In: Proceedings of the 20th International Conference on Soil Mechanics and geotechnical Engineering, 2022b.

Monforte, L., Arroyo, M., Gens, A. “Undrained strength from CPTu in brittle soils: a numerical perspective”. In: Proceedings of the 5th International Symposium on Cone Penetration Testing (CPT’22), Bologna, Italy, 2022c. http://doi.org/10.1201/9781003308829-85

Monforte, L., Arroyo, M., Gens, A. “A relation between undrained CPTu results and the state parameter for liquefiable soils”, Canadian Geotechnical Journal, 60(11), pp. 1756-1774, 2023a. https://doi.org/10.1139/cgj-2022-0377

Monforte, L., Arroyo, M., Gens, A. “Cone penetration in brittle, lightly over-consolidated soils: a numerical perspective”, In: 10th European Conference on Numerical

Methods in Geotechnical Engineering, London, United Kingdom, pp 1-6, 2023b. https://doi.org/10.53243/NUMGE2023-125

Monforte, L., Arroyo, M., Gens, A. "Numerical simulation of soil structure damage upon sampling". In: 8th International Symposium on Deformation Characteristics of Geomaterials (ISDCG2023), 2023c.

Monforte, L., Collico, S., Arroyo, M., Gens, A. "State parameter from undrained CPTu: a comparison of interpretation techniques", under review, 2024.

Mozaffari, M., Ghafghazi, M. "Material-specific interpretation of the state parameter from drained cone penetration test", ahead of print, 2024. https://doi.org/10.1139/cgj-2022-0490

Nazem, M., Carter, J.P., Airey, D.W., Chow, S.H. "Dynamic analysis of a smooth penetrometer free-falling into uniform clay", Géotechnique, 62(19), pp. 893-905, 2012. https://doi.org/10.1680/geot.10.P.055

Nazem, M., Sheng, D., Carter, J.P., Sloan, S.W. "Arbitrary-Lagrangian-Eulerian method for large-deformation consolidation problems in geomechanics", International Journal for Numerical and Analytical Methods in Geomechanics, 32, pp. 1023-1050, 2008. https://doi.org/10.1002/nag.657

Oliver, J., Cante, J.C., Gonzalez, C. "On particle finite element methods in solid mechanics problems". In Computational Plasticity: Fundamentals and Applications - Proceedings of the 8th International Conference on Computational Plasticity, COMPLAS VIII, pp. 82–85, 2005.

Oliver, J., Huespe, A.E., Cante, J.C. "An implicit/explicit integration scheme to increase computability of non-linear materials and contact/friction problems", Computer Methods in Applied Mechanics and Engineering, 197(21-24), pp. 1865-1889, 2008. https://doi.org/10.1016/j.cma.2007.11.027

Oñate, E., Idehsohn, S.R., del Pin, F., Aubry, R. "The particle finite element method – an overview", International Journal of Computational Methods, 1(2), pp. 267-307, 2004. https://doi.org/10.1142/S0219876204000204

Paniagua, P., D'Ignazio, M., L'Heureux, J.-S., Lunne, T., Karlsrud, K. "CPTU correlations for Norwegian clays: an update". AIMS Geosciences, 5(2): 82-103, 2009. http://doi.org/0.3934/geosci.2019.2.82

Peuchen J, Vanden Berghe J.F., Coulais, C. "Estimation of u1/u2 conversion factor for piezocone". In: CPT'10, 2nd International Symposium on Cone Penetration Testing, 1-03, 2010.

Pezeshki, A., Ahmadi, M.M. "In situ state of tailing silts using a numerical model of piezocone penetration test developed by Norsand model", International Journal of Geomechanics, 22(1), 04021264, 2022. https://doi.org/10.1061/(ASCE)GM.1943-5622.0002250

Plewes, H.D., Davies, M.P., Jefferies, M.G. "CPT based screening procedure for evaluating liquefaction susceptibility". In: Proceedings of the 45th Canadian Geotechnical Conference, Toronto, Canada, 1992.

Robertson, P.K. "Soil classification by the cone penetration test: Reply", Canadian Geotechnical Journal, 28(1), pp. 176-178, 1991. https://doi.org/10.1139/t91-024

Rodríguez, J. M., Carbonell, J.M., Cante, J.C., Oliver, J. "The particle finite element method (PFEM) in thermo-mechanical problems", International Journal for Numerical Methods in Engineering, 107(9), pp. 733–785, 2016. https://doi.org/10.1002/nme.5186

Rouainia, M., Muir Wood, D. "A kinematic hardening constitutive model for natural clays with loss of structure", Géotechnique, 50(2), pp. 153-164, 2000. https://doi.org/10.1680/geot.2000.50.2.153

Sagaseta, C., Whittle, A.R., Santagata, M., "Deformation analysis of shallow penetration in clay", International Journal for Numerical and Analytical Methods in Geomechanics, 21(10), pp. 687-719, 1998. https://doi.org/10.1002/(SICI)1096-9853(199710)21:10%3C687::AID-NAG897%3E3.0.CO;2-3

Santagata, M., Sinfield, J.V., Germaine J.T. "Laboratory simulation of field sampling: comparison with ideal sampling and field data", 132(3), pp. 351-362, 2006. https://doi.org/10.1061/(ASCE)1090-0241(2006)132:3(351)

Schneider, J., Randolph, M.F., Mayne, P.W., Ramsey, N.R. "Analysis of factors influencing soil classification using normalized piezocone tip resistance and pore pressure parameters", Journal of Geotechnical and Geoenvironmental Engineering, 134(11), pp. 1569-1586. https://doi.org/10.1061/(ASCE)1090-0241(2008)134:11(1569)

Sheng, D., Kelly, R., Pineda, J., Bates, L. "Numerical study of rate effects in cone penetration test", In: 3rd International Symposium on Cone Penetration Testing, Las Vegas, USA, 2014.

Sheng, D., Cui, L., Ansari, Y. "Interpretation of cone factor in undrained soils via full-penetration finite element analysis", International Journal of Geomechanics, 13(6), pp. 745-753, 2013. https://doi.org/10.1061/(ASCE)GM.1943-5622.0000279

Shuttle, D.A., Cunning, J. " Liquefaction potential of soils from CPTu", Canadian Geotechnical Journal, 44, pp. 1–19, 2007. https://doi.org/10.1139/t06-086

Shuttle, D., and Jefferies, M. "Determining silt state from CPTu". Geotechnical Research, 3(3), pp. 90–118, 2016. https://doi.org/10.1680/jgere.16.00008

Siddique, A., Farooq, S.M., Clayton, C.R.I. "Disturbance due to tube sampling in coastal soils", Journal of Geotechnical and Geoenvironmental Engineering, 126(6), pp. 568-575, 2000. https://doi.org/10.1061/(ASCE)1090-0241(2000)126:6(568)

Simo, J.C., Hughes, T.J.R. "Computational Inelasticity", Springer, New York, United States, 1998. https://doi.org/10.1007/b98904

Sloan, S.W., Abbo, A.J., Sheng, D. "Refined explicit integration of elastoplastic models with automatic error control", Engineering computations, 18(1/2), pp. 121-154, 2001. https://doi.org/10.1108/02644400110365842

Sun W.C., Ostien J.T., Salinger A.G. "A stabilized assumed deformation gradient finite element formulation for strongly coupled poromechanical stimulations at finite strains". International Journal for Numerical and Analytical Methods in Geomechanics, 37(16), pp. 2755–2788, 2013. https://doi.org/10.1002/nag.2161

van den Berg, P., Borst, R., Huétink, H. "An Eulerian finite element model for penetration in layered soil", International Journal for Numerical and Analytical Methods in Geomechanics, 20, pp. 865-886, 1996. https://doi.org/10.1002/(SICI)1096-9853(199612)20:12%3C865::AID-NAG854%3E3.0.CO;2-A

Vermeer, P.A., Verruijt, A. "An accuracy condition for consolidation by finite elements", International Journal for Numerical and Analytical Methods in Geomechanics, 5(1), pp. 1-14, 1981. https://doi.org/10.1002/nag.1610050103

Walker, J., Yu, H.S. "Adaptive finite element analysis of cone penetration in clay", Acta Geotechnica, 1, pp. 43-57. 2006. http://doi.org/10.1007/s11440-006-0005-9

Walker, J., Yu, H.S. "Analysis of the cone penetration test in layered clay", Géotechnique, 60(12), pp. 939-9487, 2010. https://doi.org/10.1680/geot.7.00153

Wheeler, S. J., Näätänen, A., Karstunen, M., Lojander, M. "An anisotropic elasto-plastic model for soft clays", Canadian Geotechnical Journal, 40(2), pp. 403–418, 2003. https://doi.org/10.1139/t02-119

Wriggers, P. "Computational Contact Mechanics", 2nd ed., Springer Berlin, Heidelberg, Berlin, Germany, 2006. https://doi.org/10.1007/978-3-540-32609-0

Yost, K.M., Yerro, A., Green, R.A., Martin, E., Cooper, J. "MPM modelling of cone penetrometer testing for multiple thin-layer effects in complex soil stratigraphy", Journal of Geotechnical and Geoenvironmental Engineering, 148(2),

04021189, pp. 1-17, 2022. https://doi.org/10.1061/(ASCE)GT.1943-5606.0002730

Yu, H. S. “CASM: a unified state parameter model for clay and sand”, International Journal for Numerical and Analytical Methods in Geomechanics, 22(8), pp. 621-653. https://doi.org/10.1002/(SICI)1096-9853(199808)22:8%3C621::AID-NAG937%3E3.0.CO;2-8

Zambrano-Cruzatty, L., Yerro, A. “Numerical simulation of free fall penetrometer deployment using the material point method”, Soils and Foundations, 60(3), pp. 668-682, 2020. https://doi.org/10.1016/j.sandf.2020.04.002

Zhang, N., Arroyo, M., Ciantia., M.O., Gens, A. “Energy balance analyses during Standard Penetration Tests in a virtual calibration chamber”, Computers and Geotechnics, 133, 104040, 2021. https://doi.org/10.1016/j.compgeo.2021.104040

Zhang, N., Arroyo, M., Ciantia, M.O., Gens, A., Butlanska, J., “Standard penetration testing in a virtual calibration chamber”, Computers and Geotechnics, 111, pp. 277-289, 2019. https://doi.org/10.1016/j.compgeo.2019.03.021

Zhang, X., Krabbenhoft, K., Pedroso, D.M., Lyamin, A.V., Sheng, D., Da Silva, M.V., Wang, D. “Particle finite element analysis of large deformation and granular flow problems”, Computers and Geotechnics, 54, pp. 133–142, 2013. https://doi.org/10.1016/j.compgeo.2013.07.001

Zhang, X., Krabbenhoft, K., Sheng, D. “Particle finite element analysis of the granular column collapse problem”, Granular Matter, 16 (4), 609–619, 2014. https://doi.org/10.1007/s10035-014-0505-5

Zhou, H., Randolph, M.F. “Resistance of full-flow penetrometers in rate-dependent and strain-softening clay”, Géotechnique, 59(2), pp. 79-86, 2009.

Zienkiewicz, O.C., Chan, A.H.C, Pastor, M., Schrefler, B.A., Shiomi, T. “Computational Geomechanics with Special Reference to Earthquake Engineering”, 1st ed, John Wiley & Sons, 1999. https://doi.org/10.1680/geot.2007.00164

Zienkiewicz, O.C., Taylor, R.L. “The Finite Element Method: its basis and fundamentals”, Butterworth-Heinemann, 2013. https://doi.org/10.1016/C2009-0-24909-9